SANDIA REPORT

SAND2020-10650
Unlimited Release
Printed September, 2020

Designing Catalysts for Dehydrogenation of Methane for Reducing Greenhouse Gas during Natural Gas Extraction

Quinn Campbell, Peter A. Schultz, Kevin Leung

Prepared by
Sandia National Laboratories
Albuquerque, New Mexico 87185 and Livermore, California 94550

Sandia National Laboratories is a multimission laboratory managed and operated by National Technology and Engineering Solutions of Sandia, LLC., a wholly owned subsidiary of Honeywell International, Inc., for the U.S. Department of Energy's National Nuclear Security Administration under contract DE-NA0003525.

Sandia National Laboratories

Issued by Sandia National Laboratories, operated for the United States Department of Energy by National Technology and Engineering Solutions of Sandia, LLC.

Available to DOE and DOE contractors from
U.S. Department of Energy
Office of Scientific and Technical Information
P.O. Box 62
Oak Ridge, TN 37831

Telephone: (865) 576-8401
Facsimile: (865) 576-5728
E-Mail: reports@adonis.osti.gov
Online ordering: http://www.osti.gov/bridge

Available to the public from
U.S. Department of Commerce
National Technical Information Service
5285 Port Royal Rd
Springfield, VA 22161

Telephone: (800) 553-6847
Facsimile: (703) 605-6900
E-Mail: orders@ntis.fedworld.gov
Online ordering: http://www.ntis.gov/help/ordermethods.asp?loc=7-4-0#online

SAND2020-10650
Unlimited Release
Printed September, 2020

Designing Catalysts for Dehydrogenation of Methane for Reducing Greenhouse Gas during Natural Gas Extraction

Quinn Campbell, Peter A. Schultz, Kevin Leung

Abstract

Catalytic conversion of methane (CH_4) into useful products is critical for maximizing the utility of natural gas output and for reducing green house gas release associated with flaring (burning off CH_4 at natural gas extraction sites). One particular useful technique is methane dry reforming (DRM), which involves the chemical reaction of CH_4 with carbon dioxide (CO_2) to generate carbon monoxide (CO), hydrogen gas (H_2), and subsequently other useful products. New and improved catalysts are required to facilitate efficient dry methane reforming. In this report, we apply the Density Functional Theory (DFT) computational technique to investigate a catalyst consisting of small nickel clusters (Ni_n, n<10) on ceria (CeO_2 (111) surfaces) support. One main thrust of this project is to study the initial CH_4 and CO_2 reactions with the catalyst. We find that CH_4 exhibits barrierless reactive adsorption on to the catalyst. In order words, this step is likely not the rate-determining step. A second thrust is to perform detailed studies of the catalyst itself and examine the role of oxygen vacancies. Using a specific DFT method and a hypothesis about the absence of the Ce(III) redox state, we obtain predictions about oxygen vacancies in good agreement with experimental observations.

Acknowledgment

We are grateful to Andrew Baczewski for useful discussions on the direction of the work. We also thank Ariana Beste, Daniel Janssen, and Christopher Riley for useful suggestions.

Contents

List of Figures

List of Tables

Chapter 1

CH_4 and CO_2 Catalytic Reactions

Introduction

Rising methane emissions pose a serious concern for the climate, with methane having approximately 25 times the short term warming impact of carbon dioxide.[1] Substantial amounts of methane are currently emitted as waste in both the fracking of natural gas and as a natural byproduct of farming.[2, 3] Ideally, this waste methane could be captured and then converted to other useful hydrocarbon forms that could be directly used for energy production. Dry reformation of methane (DRM) provides a process for converting methane and carbon dioxide into a mixture of carbon monoxide and hydrogen gas known as syngas.[4, 5] This syngas is an important chemical precursor for later catalytic conversion using the Fischer-Troph process.[6] The widespread application of DRM at methane emission hotspots could therefore substantially increase energy efficiency of methane usage and decrease both short term climate impacts from methane and long term impacts from carbon dioxide.

DRM has not yet been widely deployed, however, due to a number of outstanding challenges making the process impractical. DRM is a highly intricate process with at least six main reactions and dozens of side reactions.[7] Many of these reactions require high temperatures, with a typical operating temperature around $\sim$400 °C.[8] Understanding which of these reactions are rate limiting steps is crucial to improving the performance of next generation DRM devices. Furthermore, the exact design of both catalyst and support can make a large difference on the overall efficiency of DRM by influencing these rate limiting steps.[9] While a wide variety of catalyst and supports have been explored, nickel nanoparticle catalysts with a ceria (CeO_2) support have shown excellent performance for DRM and other similar catalytic reactions.[8, 10, 11, 12]

Accordingly, researchers have significantly explored the Ni nanoparticle with ceria support system for DRM using a variety of theoretical methods. Density functional theory (DFT) analysis has been widely used to find the most stable structures of Ni nanoparticles on both stable and reduced ceria, from the adsorption site for a single Ni atom through nanoparticles of up to 20 Ni atoms.[13, 14, 15, 16, 17] It is important to note that while these lowest energy structures can be useful guidelines, given the high temperature of operation, it is likely that several metastable configurations comfortably coexist. The consensus is that nanoparticles are generally favored to sinter into larger clusters.[15, 16]

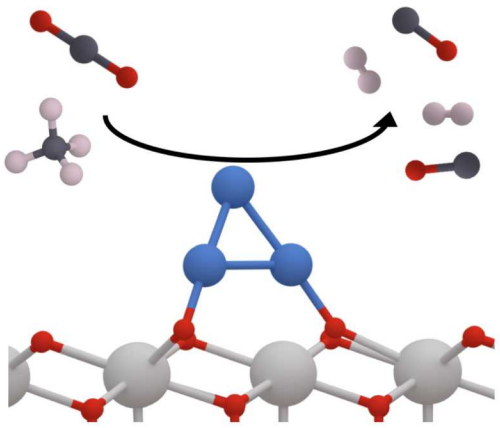

Figure 1.1. A cartoon illustration of the dry reformation of methane process (DRM). Methane (CH_4) and carbon dioxide (CO_2) are exposed to a catalyst, here illustrated as a ceria (CeO_2) supported nickel nanoparticle catalyst. Through a series of chemical reactions at temperatures $\gtrapprox 400\,^{\circ}\mathrm{C}$, these inputs are then transformed into syngas, a mixture of carbon monoxide (CO) and hydrogen gas (H_2).

After nickel nanoparticle formation, the initial adsorption and methane has been the most studied step as it is often assumed within the DRM community that the initial dissociation of CH_4 to CH_3 + H will be the rate limiting step, as seen for pure Ni and Pt catalysts.[18, 19, 20] DFT calculations are typically limited to a subset of the possible Ni nanoparticle sizes, often focused on 1 or 4 Ni atom structures, finding barriers to methane dissociation on the order of ~ 0.7 eV.[21, 22] Lustemberg *et al.* have experimentally measured methane dissociation at room temperature on ceria supported nickel nanoparticles.[8, 23] Lian *et al.* have recently shown on an 8 Ni cluster that the exact location of dissociation (on the support, on the nanoparticle, at the interface) can have a significant impact on the ultimate barrier for both methane and carbon dioxide dissociation.[24] None of these works have systematically examined how methane and carbon dioxide adsorption and dissociation may change as the Ni nanoparticle size is increased. Given the predicted tendency of Ni to sinter into large clusters, understanding this trend may be vital to understanding the real world behavior of these systems.

In this paper, we use DFT with a Hubbard U correction (DFT+U) to examine the initial adsorption and dissociation of both methane and carbon dioxide as a function of Ni nanoparticle size on a ceria support. We find barrierless dissociation of methane from CH_4 to CH_3* + H* at all Ni nanoparticle sizes tested. We further show that carbon dioxide has a more favorable adsorption energy directly on the nickel nanoparticle than at the nickel–ceria interface, which may lead to lowered barriers for initial dissociation. We thus conclude that both the initial dissociation of methane and carbon dioxide are unlikely to be the rate limiting step of DRM in a ceria supported nickel system, regardless of the size of the underlying nickel

particles.

Methods

To model Ni nanoparticles with a ceria support, we generate a 2 x 2 ceria slab in the (111) direction with five layers and 20 Å of vacuum space between sides to eliminate any spurious surface interactions. To discover the configuration of Ni nanoparticles, we start with a clean ceria surface, adding one Ni atom at several positions on the surface, measuring adsorption energy of the Ni atom on the surface as

$$E_{\mathrm{a,Ni_x}} = E_{\mathrm{CeO_2/Ni_x}} - E_{\mathrm{CeO_2/Ni_{x-1}}} - E_{\mathrm{Ni_1}}, \tag{1.1}$$

where $E_{\mathrm{CeO_2/Ni_x}}$ is the DFT calculated energy of the ceria slab with an x Ni atom nanoparticle adsorbed, and $E_{\mathrm{Ni_1}}$ is the DFT calculated energy of a single Ni atom surrounded by a 15 Å wide cube of vacuum. Once the lowest energy configuration is found for a given x atom Ni nanoparticle, we then begin again by adding an additional Ni atom and determining its lowest energy configuration.

With equilibrium configurations for the Ni nanoparticles in hand, we then introduce methane and carbon dioxide molecules to the surface, measuring the adsorption energy for a particular nanoparticle Ni_x as:

$$E^{\mathrm{Ni_x}}_{\mathrm{a,molecule}} = E^{\mathrm{Ni_x}}_{\mathrm{CeO_2/molecule}} - E^{\mathrm{Ni_x}}_{\mathrm{CeO_2}} - E_{\mathrm{molecule}}, \tag{1.2}$$

where $E^{\mathrm{Ni_x}}_{\mathrm{CeO_2/molecule}}$ is the DFT energy of the molecule adsorbed onto a ceria slab with a Ni_x nanoparticle, $E^{\mathrm{Ni_x}}_{\mathrm{CeO_2}}$ is the DFT energy of the ceria slab with a Ni_x nanoparticle and no adsorbate, and E_{molecule} is the energy of the molecule calculated isolated in a 15 Å wide cube of vacuum.

All electronic structure calculations are performed using the plane wave QUANTUM-ESPRESSO software.[25] The bottom two layers of the slab are frozen and the geometry of the surface layers along with the adsorbate are relaxed until the interatomic forces are lower than 50 meV/Å. We use norm-conserving pseudopotentials with Perdew-Burke-Ernzerhof exchange correlation [26] from the SSSP precision repository.[27, 28] We use kinetic energy cutoffs of 80 Ry and 640 Ry for the plane wave basis sets used to describe the Kohn-Sham orbitals and charge density, respectively. We sample the Brillouin zone with a 2 x 2 x 1 Monkhorst-Pack grid[29] and 0.01 Ry of Marzari-Vanderbilt smearing.[30] Spin polarization has been included in all calculations.

We utilize a Hubbard U potential on the cerium atom to counteract the unphysical electronic delocalization of the f orbital within standard density-functional theory. It should be noted that there is discussion in the literature on the exact value of U that should be used for a ceria surface depending on application.[31, 32] Following Hahn *et al.* and other examples[15, 23, 33, 24] attempting to understand the ceria supported nickel system within the literature, we set the value of the cerium U to 4.5 eV.

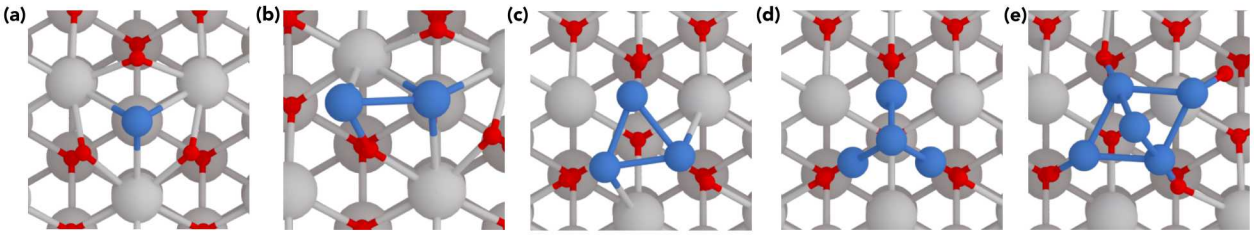

Figure 1.2. A top view of our predicted Ni nanoparticle structures for (a) 1 Ni atom, (b) 2 Ni atom, (c) 3 Ni atom, (d) 4 Ni atom, and (e) 5 Ni atom. These configurations should not be taken as the absolute lowest energy configurations, but one of many reasonably likely configurations likely to coexist at typical DRM operating temperatures.

Reaction barriers are calculated using the Nudged Elastic Band (NEB) method as implemented within the QUANTUM-ESPRESSO package.

Results and Discussions

Differing nanoparticle size

For our calculations of methane and carbon dioxide adsorption, we use the configuration of nickel nanoparticles on an unmodified ceria surface shown in Fig. 1.2. Nickel nanoparticle structure shapes are found to align qualitatively well with other works. A single nickel atom adsorbs at the hollow site above an oxygen atom. We predict a relatively high adsorption energy of –3.93 eV, as shown in Fig. 1.3. A second Ni atom then attaches in a bridging position between a nearby Ce and O atom with an adsorption energy of –3.58 eV. This is less than the adsorption energy of a single Ni atom, indicating that a Ni atom adsorbing onto the surface may prefer to adsorb as a single atom nanoparticle at another site versus combining into a two atom nanoparticle in this configuration. It should be noted that as the focus of this paper is not on determining the equilibrium position of nickel nanoparticles as a function of size, the search for nanoparticle configurations was not exhaustive and lower energy configurations may exist. This result should instead be taken as indicative of one of many favorable nanoparticle configurations. Given the elevated temperature of operation, there will likely be several potential configurations in coexistance at any given moment.

Above two atoms, we always find it favorable to add additional Ni atoms to a nanoparticle. We predict a triangular three Ni atom nanoparticle shape, centered at the oxygen hollow site and with all Ni atoms pointing to one of the nearby oxygen atoms. From there, a four Ni atom nanoparticle forms as a pyramid, with the additional atom adsorbing on top of the established three atom triangular structure. We finally predict a five Ni nanoparticle to form

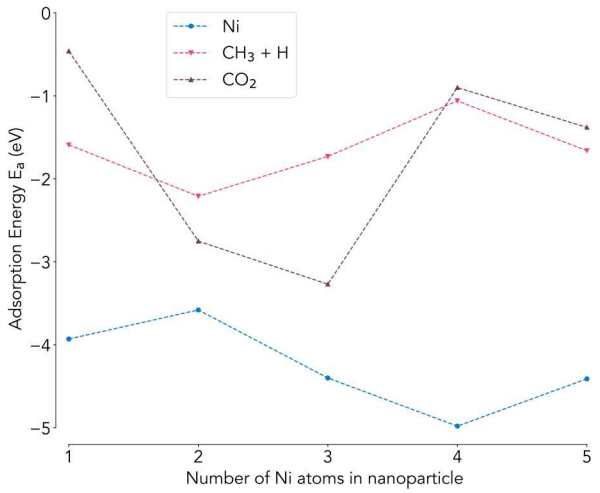

Figure 1.3. The adsorption energy of an additional nickel atom onto a larger nickel nanoparticle, the dissociated CH_3 + H configuration, CO_2 adsorbed at the the interface of the nickel nanoparticle and the ceria support, and CO_2 directly adsorbed on the nickel nanoparticle.

as an extended pyramid, with a new corner stretching to the neighboring Ce hollow site and the on top Ni atom moving in between the two middle base atoms.

The high adsorption energy of nickel nanoparticles at all sizes indicates that these nanoparticles will stay firmly attached to the ceria system once adsorbed, even at the elevated temperatures of typical DRM operation. Our results also match the previous findings that nickel clusters are indeed thermodynamically favorable to sinter into larger nanoparticles. We next investigate how methane and carbon dioxide dissociation are affected by this likely change in nickel nanoparticle size.

Methane adsorption and decomposition

Methane dissociation has traditionally been thought of as the rate limiting step in DRM. In both pure metals of Pt and Ni, the barrier to the initial dissociation of CH_4* to CH_3* + H* has been shown to dominate the reaction pathway.[18, 19]

We predict a pathway from methane gas to adsorbed CH_3* + H* that does not require an intermediate adsorbed CH_4 step and therefore eliminates the initial barrier to dissociation for methane gas adsorbing onto the surface. It is important to note that this pathway does not eliminate the possibility of a barrier for dissociation once the methane molecule has *already* been adsorbed. The location of the final adsorbed CH_3* and H* for each Ni nanoparticle configuration is shown in Fig. 1.4. In this path, the methane adsorbs on the

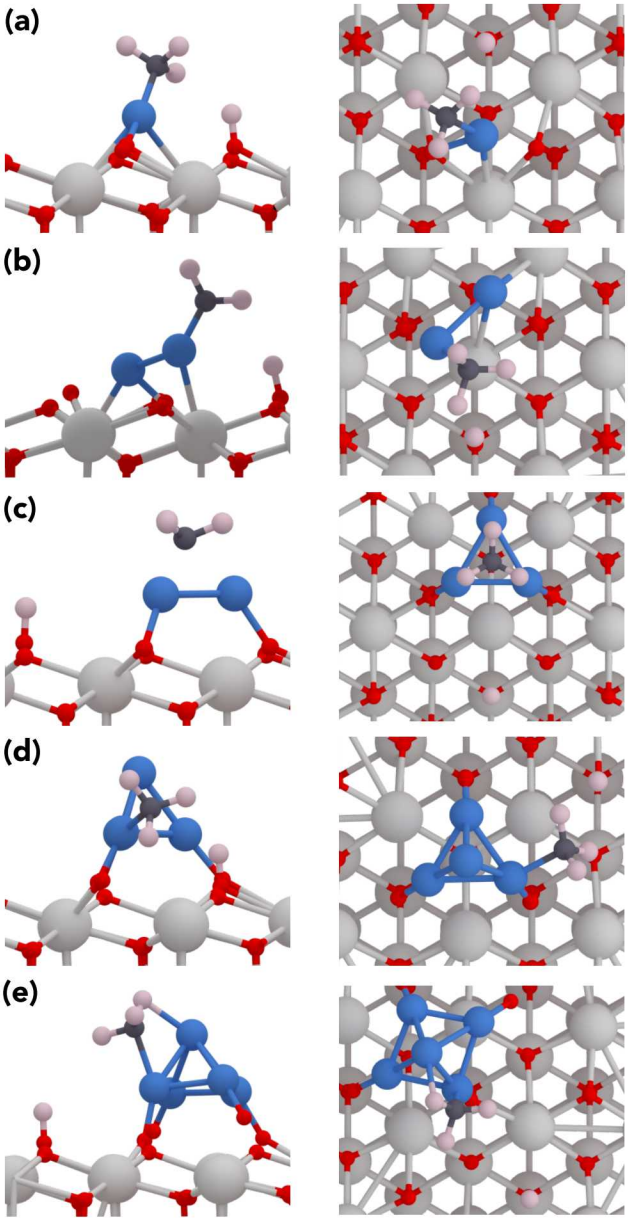

Figure 1.4. The final adsorbed configuration of CH_3* + H on the ceria supported nickel nanoparticles. Both side and top views are shown for (a) 1 Ni atom, (b) 2 Ni atom, (c) 3 Ni atom, (d) 4 Ni atom, and (e) 5 Ni atom nanoparticles. These dissociation pathways are all found to occur without a barrier from CH_4 gas.

edge of the nickel nanoparticle, interacting with both the nanoparticle and the ceria surface. This qualitatively matches recent work by Lian *et al.* that showed the metal support interface to have the lowest barriers to methane and carbon dioxide activation.[24] The CH_3* fragment adsorbs onto the nickel nanoparticle and then the remaining hydrogen atom gets adsorbed onto a nearby oxygen atom on the ceria surface.

Furthermore, this dissociation pathway for methane gas is not dependent on the size of the nickel nanoparticle, suggesting that it will be resilient to further sintering of the Ni nanoparticle. The adsorption energy of the dissociated CH_3* + H* starts at –1.59 eV for a one nickel atom nanoparticle. This adsorption energy then decreases to a minimum for the two nickel atom structure before increasing to its least stable form for the 4 Ni nanoparticle structure at –1.06 eV. The adsorption energy then decreases again to be more stable for a 5 Ni nanoparticle. This pathway does require, however, that the initial approach of the methane gas molecule to be near the metal support interface, as opposed to on top of the nickel or directly on the ceria surface. It may thus be expected that as nickel atoms on the ceria surface sinter into larger nanoparticles that extend more vertically than horizontally, the amount of exposed pure nickel will increase and the chances of barrierless dissociation will decrease. Strategies for maximizing CH_4 dissociation at low temperatures should focus on ensuring that the maximum amount of metal support interface is exposed.

This barrierless dissociation of methane could have significant impacts on the study of ceria supported nickel nanoparticle catalysts for DRM. Recent experimental evidence has demonstrated the initial methane dissociation step being accomplished at room temperature,[23] matching our predictions well (although merely low barriers are required for room temperature activation, not necessarily no barrier). Nonetheless, effective DRM still requires temperatures on the order of 400 °C. This implies that the initial dissociation of methane is not, in fact, the rate limiting step for DRM.

There remains several possibilities that could serve as rate limiting steps. As discussed above, the sintering of large nickel nanoparticles could reduce the chances of the barrierless pathway occurring at higher temperatures. Similarly, we do not test the further dissociation of CH_3*, which indeed, once already adsorbed onto the nickel nanoparticle, requires overcoming several barriers to fully dehydrogenate. Significant accumulation of carbon is also a well known factor in reduced performance and could be likely to accumulate through intermediary reactions and block pathways for easy dissociation. Alternatively, the rate limiting factor could instead be found in the decomposition of carbon dioxide. In the next section, we investigate the initial adsorption of carbon dioxide to examine this possibility.

Carbon dioxide adsorption

The literature has largely settled on a "bifunctional" process to describe DRM on the ceria supported nickel system where methane is dissociated at the nickel nanoparticle-ceria interface, and carbon dioxide is dissociated at the ceria surface, with its substantial oxygen reservoir.[34] Lian *et al.* have shown, however, that carbon dioxide dissociation is possible

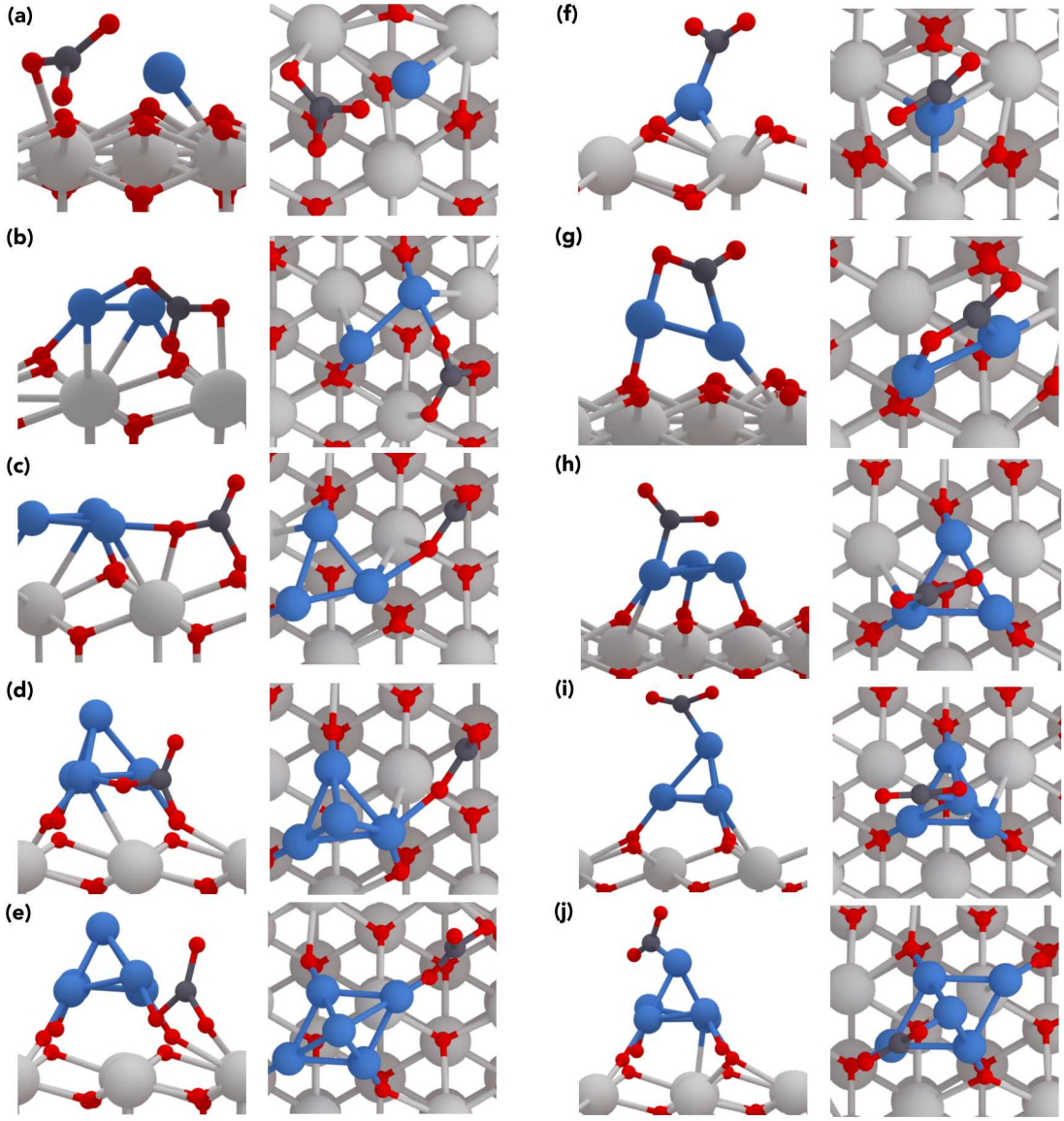

Figure 1.5. The positions of initial carbon dioxide adsorption. Both side and top views are available for carbon dioxide adsorption at the nickel nanoparticle ceria interface on (a) 1 Ni atom, (b) 2 Ni atom, (c) 3 Ni atom, (d) 4 Ni atom, and (e) 5 Ni atom nanoparticles. Carbon dioxide shows a consistently stronger adsorption, however, when adsorbing directly onto the nickel nanoparticle as shown for (f) 1 Ni atom, (g) 2 Ni atom, (h) 3 Ni atom, (i) 4 Ni atom, and (j) 5 Ni atom nanoparticles.

at the metal–support interface as well as directly on top of the metal and at any oxygen vacancy cite.[24] In this work we examine both the interface between the nickel nanoparticle and the ceria surface and directly on the nickel nanoparticle as locations for initial carbon dioxide adsorption.

Carbon dioxide has a systematically stronger adsorption energy directly on top of the nickel nanoparticle than at the interface between the nickel nanoparticle and the supporting ceria, as demonstrated in Fig. 1.3. For most nanoparticle sizes, the carbon dioxide is ∼1 eV more likely to adsorb directly on the nanoparticle as opposed to the interface. The exception to this trend is the 2-Ni nanoparticle, in which the difference between the two sites is only 0.2 eV. For the interfacial carbon dioxide, the adsorption energy thus reaches its lowest and strongest point for a 2 Ni atoms, and increases as the Ni atom size increases. In contrast, for the adsorption directly onto the nickel nanoparticle, the adsorption energy reaches its minimum at 3 Ni atoms.

One potential explanation for the decreased adsorption of carbon dioxide at the interfacial sites is that the carbon dioxide tends to pull oxygen from the ceria surface toward the carbon, as illustrated in Fig. 1.5. This reduces the symmetry of the surface, and pushes the oxygen surrounding the carbon dioxide into a trigonal-planar formation. This interfacial structure remains consistent regardless of the nickel nanoparticle size, indicating that this will likely remain a stable feature even if the nickel sinters to larger structures. Carbon dioxide adsorbs with less distortion when landing directly on the nickel nanoparticle, with no change in the underlying structure and a bending of the oxygen angle.

This difference in adsorption energy may also imply a lower reaction barrier for initial carbon dioxide dissociation. Lian *et al.* have shown that the reaction barrier for CO_2* dissociating into CO* + O* is $\sim$ 0.8 eV lower directly on the nickel nanoparticle as opposed to at the nickel ceria interface. [24] Our work implies that the carbon dioxide is most likely to adsorb directly on the nickel, making the dissociation process more likely to occur at low thermal budgets. Furthermore, this result is independent of nickel nanoparticle size and will not be affected by sintering, although sintering into larger particles where many of the nickel atoms are "hidden" in the lower layers of the nanoparticle structure may reduce the surface area where carbon dioxide can easily adsorb directly onto the nickel as opposed to dispersed nickel atoms

Due to resource restrictions, we did not investigate the impact of oxygen vacancies on carbon dioxide adsorption and dissociation, which is known to play a significant role within any ceria based DRM system. Our results should therefore not be taken as a definitive stance on the dissociation of carbon dioxide, but illustrative of the general impact of changing nickel nanoparticle size on initial adsorption. In general, oxygen vacancies can be expected to further decrease the barrier to carbon dioxide dissociation.

The role of DFT+U should also be noted. Previous work on this system using DFT+U has provided a wide range of adsorption energies even for the same U value. It is possible that our DFT+U value leads to overbinding and thus an underestimation of the barriers required for dissociation. Given the extremely downhill nature of the methane dissociation

reaction reported here, we expect the impact to be minimal, but it is worth further work exploring how robust this finding is to the exact DFT+U settings used.

We thus conclude that the rate limiting step of DRM on ceria supported nickel is unlikely to be either initial methane dissociation or carbon dioxide adsorption, at least at low nickel nanoparticle sizes. While we do not find any changes in the barrierless dissociation of methane or the preference for direct on metal carbon dioxide adsorption as a function of nanoparticle size, it is possible that changes in nanoparticle size may make these pathways less easily accessible, by reducing the area of the nickel–ceria interface or the available nickel atoms to directly attach to. Further research on this subject to find the rate limiting step of DRM in this system should likely focus attention on the several intermediary reactions after initial dissociation that lead to syngas formation, along with the sintering of nickel into even larger particles

Conclusion

In this work, we use first principles DFT+U methods to examine the impact of changing nickel nanoparticle size on the initial adsorption/dissociation of methane and carbon dioxide. We find nickel nanoparticle structures consistent with literature and find a minimum adsorption energy at 4 Ni atoms. We discover a novel pathway for the barrierless dissocciation of CH_4 to CH3* + H* at the interface of the nickel nanoparticle with the ceria support that is independent of the number of nickel atoms, but does require methane to adsorb at the nickel–ceria interface. Strategies for maximizing the amount of exposed metal support interface are therefore likely to lead to enhanced low temperature performance. We examine the initial adsorption of carbon dioxide, demonstrating a consistently lower adsorption energy for carbon dioxide directly adsorbing onto the nickel nanoparticle. This implies that lower energy barriers may be easily accessible for carbon dioxide dissociation. Overall, our work shows that the initial dissociation of methane and carbon dioxide is unlikely to be the rate limiting step of DRM on the ceria supported nickel system. These findings are robust at all nickel particle sizes tested, but the possibility remains that further sintering of the system may make the pathways outlined above less accessible. We conclude that future work should instead focus on the numerous intermediary reactions and the potential impact of coking to find the true rate limiting step.

Chapter 2

Catalyst Modeling

Using first-principles density functional theory methods, we explore the fundamental materials aspects that endow a ceria-supported nickel catalyst system with its special bi-functional catalytic properties. The elevated operation temperatures of the system prove to be an essential aspect of not just enabling the chemistry, but also of activating key processes of this catalytic foundation. The crucial dispersion of metal catalyst is found to be stabilized by the existence of "magic cluster" sizes, toward which an adsorbed population of nickel will ripen at high temperatures. The redox capability of the ceria substrate is fueled by the facile, but not too facile, transport of oxygen atoms: neutral oxygen vacancies are found to migrate through a subsurface reservoir with moderate barriers. In contrast with the conventional approaches that use DFT+U or hybrid functionals to circumvent an unphysical delocalization of the electrons in an oxygen vacancy and impose a localization into a Ce $4f$ state, our simulations are performed with standard density functionals, where unphysical delocalization is instead avoided by explicitly preventing occupation of a Ce $4f$ state.

Introduction

Transition metals dispersed on an oxide support (substrate surface) are fascinating materials systems, of great value to vital chemical processes such as catalysis. Oxide-supported metal systems' facility for sophisticated catalysis, such as for the immensely valuable chemical process of dry reforming of methane (DRM),

$$\mathrm{CH_4} + \mathrm{CO_2} \rightarrow 2\ \mathrm{CO} + 2\ \mathrm{H_2}, \tag{2.1}$$

is often attributable to a "bi-functional" mechanism.[34] In the case of DRM, one specie, the methane, is activated (cleaved) by the adsorbed transition metal, while the other, in this case the CO_2, is activated upon the oxide, through the easy removal (reduction) and deposition (oxidation) of an oxygen atom from the oxide substrate. The subsequent chain of reaction mechanisms leading to CO and H_2[8] follows from these initial steps.

For greatest activity, the metal adsorbates should be widely dispersed, to maximize access to the metal and maximize the perimeter length that allows these bifunctional mechanisms to interoperate.. A better understanding of this chemistry, toward improving the activity and selectivity for specific chemistries,[16] is an important research area in chemistry. In this

paper, we focus on gaining fundamental understanding of the essential aspects in an oxide-supported materials system responsible for its effectiveness as a high-temperature catalytic platform.

Ceria (CeO_2) is a particularly useful oxide support material; notably for its easy storage, release, and transport of oxygen, necessary to fuel oxidation-reduction reactions at the surface; and also for its high thermal stability as a support, necessary to survive the high temperature (700-1100K) operation typical of interesting catalytic chemistry applications. Oxygen vacancies play a pivotal role in the chemistry. Facile creation and healing of oxygen vacancies at or near the ceria surface is generally believed to be an essential enabling mechanism for the catalytic behavior of the support.[35, 36, 37] The nature of these oxygen vacancies and, especially, how these vacancies might participate in the chemistry at the surface, is poorly understood.

In the search for more abundant and less expensive alternatives to supported metal catalysts such as Pt, Pd, Rh, or Pd,[37] and to survive deactivation at high temperature (these noble metals sinter, *i.e.*, un-disperse into catalytically inactive clumps), nickel has proven to be a promising candidate.[8, 15, 16, 21, 24, 38]

For the rational design of an improved oxide-supported metal catalyst system, the interaction of this oxide support with the metal adsorbates is crucial, so as to attain a catalytically effective dispersed metal catalyst. The greater the dispersion, the greater the effective area for metal-catalyzed activation. Large clusters foul by coking (carbon formation), deactivating the catalyst. Venerable models for supported metal catalysts, such as strong metal–support interactions (SMSI) or interfacial metal-support interactions (IMSI),[39], rationalize the existence of clusters, but do not explain the stability of metal clusters against sintering. The mechanisms by which a dispersed metal is achieved and sustained in chemically aggressive environments is not understood, and the effect that defects (vacancies) in the substrate might have in this stabilization is unknown.

For calculations of extended bulk or surface systems, density functional theory (DFT) methods are the current state-of-the-art for elucidating atomic-scale understanding. An accurate treatment of cerium and nickel with oxygen poses unresolved challenges for DFT, most prominently (but not exclusively) stemming from dual oxidation states accessible to Ce. The Ce typically can adopt either a nominally [4+], Ce^{IV}, with the $4f$ shell empty, or a [3+] oxidation state, Ce^{III}, with a single electron in the $4f$, a case of a highly-localized single electrons that DFT handles particularly poorly.

Ceria adopts a fluorite crystal structure, as depicted in Figure 2.1(a). In this paper, "ceria" is deemed synonymous with the fluorite structure CeO_2, the subject of this work (ignoring the Ce_2O_3 oxide). In this CeO_2 crystal, the Ce straightforwardly adopts a nominally [4+] oxidation state Ce^{IV}, counterbalanced by two nominally O[2-] ions.

The ambiguity arises when the ceria is reduced, *i.e.* oxygens are removed. First-principles DFT incorrectly gives a metallic ground state for reduced ceria surfaces,[40, 41, 42] delocalizing the two electrons left behind by an oxygen vacancy into a state distributed widely

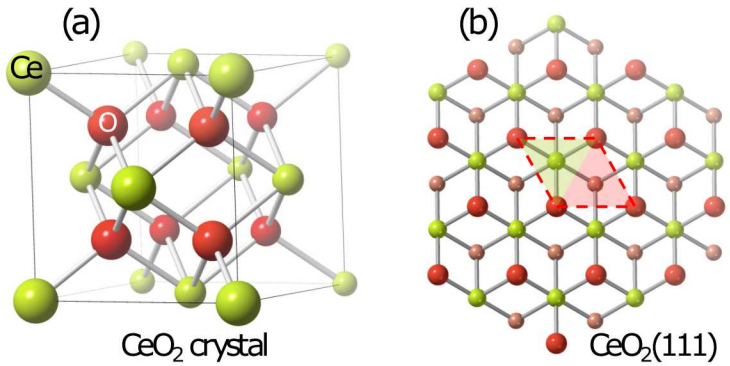

Figure 2.1. (a) Fluorite-structure crystal ceria. (b) A top-down view of the top tri-layer of the $CeO_2(111)$ surface: a top hexagonal layer of exposed oxygen atoms (large red balls), a layer of Ce below (charteuse balls), and sub-layer of O below that (small pink balls). The primitive $p(1 \times 1)$ surface cell, circumscribed by a dashed red line, is composed of two triangles, one around an underlying Ce site, the other around the sub-layer oxygen. The area depicted corresponds to the atoms of a (4×4) surface cell.

over Ce $4f$ orbitals. In nature, reduced ceria remains insulating, and the electrons around a vacancy are seen to remain localized.[43] Characterized as a "*complete* failure of the GGA approximations"[35], this prompted the use of DFT+U approaches that, with $U \sim$5 eV, eliminated the offending metallicity by localizing the distributed $4f$ state onto two Ce atoms, reducing them Ce^{IV} to Ce^{III}.[41, 42, 43] The performance of an empirical DFT+U for defects at ceria surface remained "unsatisfactory",[35] but it at least removed this fundamental failure and has been the mainstay of simulations for ceria surfaces since.

In this paper we propose and test a different hypothesis for the oxygen vacancy at the ceria surface: rather than compelling localization of the delocalized $4f$ electrons into localized $4f$-orbitals on two Ce_{III} atoms, instead, preventing any occupation of the $4f$ and thus localizing the vacancy electrons into a Coulombically bound states within the simple vacancy. This simultaneously resolves this fundamental problem in the band structure, and allows first-principles DFT to give an accurate description of the energetics of vacancies at the surfaces. This provides a consistency between theory and experimental observations for the surface and in bulk ceria that avoid contradictions with experiment observed using $+U$ approaches.

Using the (111) surface (as depicted in Figure 2.1(b)) as the substrate, we systematically examine the stability of different sized Ni nanoclusters, from one to twelve Ni atoms. We discover that the interaction of these clusters with the ceria surface imposes a steric template, through strong but somewhat adirectional Ni-O bonds, that result in "magic" clusters. These exceptionally stable cluster suggest a ripening model that could explain the generation and stability of a dispersed Ni catalysts at the CeO_2 surface at high temperatures.

The presentation begins with a description of the computational methods used, with some elaboration of the setup of the computational models. A section is devoted to the troublesome question of defining standard chemical reference states. Defining useful chemical potentials in the Ni-CeO_2 system is particularly fraught,[36, 37] and makes for difficulties benchmarking different computational studies. While formally arbitrary, we will find that judicious selection of an oxygen potential can be particularly insightful for CeO_2. A section describing the DFT results for the Ni clusters and O vacancies is followed by an analysis section that discusses the implications of the results and presents a holistic model for understanding the bifunctional oxide-supported metal catalyst.

Computational methods

Electronic structure approach

To model the behavior of transition metal atoms and vacancies at the (111) surface of the $CeO2_2$, we use first-principles density functional theory methods and a thin-film slab to approximate the semi-infinite ceria substrate.

The electronic structure calculations use the Gaussian-basis local-orbital pseudopotential code SeqQuest.[44] We use the Perdew-Burke-Ernzerhof (PBE) density functional,[26] a flavor of the generalized gradient approximation (GGA), to approximate the electron-electron interactions. Spin polarization is included in select calculations, as needed, but spin polarization mostly proves unimportant (or nonexistent) and the results reported below are spinless unless specifically stated otherwise.

Only the valence electrons are explicitly treated in these DFT calculations, the effect of core electrons replaced by generalized norm-conserving pseudopotentials (GNCPP) in the Hamann form,[45] except for the Ni atom p,d-potentials which used the Troullier-Martin form.[46] These atomic PP were generated with the FHI98PP code,[47] using custom atomic parameter settings optimized to maximize transferability.

The nickel atom PP uses an Argon core, leaving the $4s4p3d$ shells treated as valence electrons ($Z = 10$) using a $3d^8 4s^1$ ionic [1+] atomic valence state.[48] A non-linear partial-core correction (NLCC) [49] proves sufficient (in nickel) to accurately replace the core. In particular, including the semi-core $3p^6$ electrons among the valence electrons was assessed and found to be inconsequential.

The oxygen PP places the $1s^2$ into the core, and does not include a partial-core correction.

To expand the solutions of the electron wave functions, an atom-centered contracted-Gaussian "double-zeta plus polarization" (DZP) basis set is used (two radial functions for strongly-occupied atomic shells to allow for radial polarization, plus a single radial function for weakly-occupied atomic shells for angular polarization).

The cerium PP is specifically formulated to target the Ce^{IV} oxidation state, a companion to a distinct Ce^{III} PP used successfully in simulations of mechanical properties of rare-earth hydrides.[50] The valence electrons in the Ce^{IV} PP are defined by the atomic configuration of $5p^6 4f^0 5d^2 6s^1$ used to generate the PP, including the $5p^6$ semi-core electrons in the valence and using a partial core correction ($R_{NLCC} = 2.0$ Bohr) to account for remaining non-linear exchange-correlation interactions of the valence electrons with the core electrons replaced by the PP. Unlike in the Ce^{III} PP, where the $4f$ occupation was imposed through the form of the PP (the $4f^1$ shell was place explicitly in the core, preventing any change in the oxidation state, *i.e.*, imposing exactly one electron in the $4f$), the oxidation state in the Ce^{IV} atom used here is instead enforced by basis exclusion. The Ce basis set, again, is of DZP quality, but does not include f-functions to prevent occupation of the $4f$.

The DFT calculations discussed below almost universally yield an insulating electronic structure, *i.e.*, with a Fermi level inside a band gap, so that eigenstates usually can be assigned fully occupied or completely empty occupations. In certain cases, (near-)degeneracies amongst the defect states (esp. the Ni clusters) make this "closed shell" description difficult to converge. For these cases, the state occupations near the Fermi level are "smeared" with a Fermi-Dirac distribution using a (fictitious) electronic temperature that enables self-consistency to be achieved. This temperature is made small enough (usually T$\sim$0.0002 Rydberg) to not impact the total energy significantly.

To achieve total energies relaxed to within $\sim$0.01 eV of the structural minimum, atomic positions are relaxed until the forces on every (unfrozen) atom are reduced to less than 0.0003 Ry/Bohr ($\sim$0.008 eV/Å).

Computational model design

The bulk and slab ceria models are constructed and the periodic dimensions constrained to the computed equilibrium lattice constant for the fluorite structure CeO_2 (5.534 Å) using PBE functional and the Ce^{IV} atoms described above.

The defect calculations in bulk ceria are performed in 96-, 324-, and 768-site cubic supercells that are 2×2×2, 3×3×3, and 4×4×4 expansions of the conventional cubic cell (Ce_4O_8). The smaller cell uses a 3^2 regular k-grid to sample the reciprocal space in the full Brillouin Zone (BZ); a 2^2 k-grid is sufficient to converge the larger supercells (all offset from Γ). The smaller supercell might be marginally sufficient to converge the defect properties. The larger cells are used to quantify this convergence and verify extrapolations to infinitely dilute defect densities.

The workhorse computational model for the ceria(111) surface in this study is a $p(4\times4)$ slab model (the surface depicted in Figure 2.1), with five (O-Ce-O) tri-layers ("5L"), *i.e.*, fifteen atomic layers, with oxygen atoms being the top exposed layer of atoms.

The $p(4\times4)$ is the minimum lateral extent necessary to isolate the larger (*e.g.*, 10-atom) Ni-clusters from their periodic images on the surface, so as to leave at least one free surface

oxygen between the Ni clusters (Ni atoms are bonded to surface oxygens). The surface BZ of the $p(4\times4)$ and larger surface cells are sampled with a 1^2 k-mesh—the Γ-point. Smaller $p(2\times2)$ and $p(3\times3)$ surface cells use 3^2 and 2^2 k-grids, respectively. A larger lateral extent would be necessary to consider any chemistry around any one Ni-cluster, to provide free ceria surface that isolates that chemistry to one cluster, but in the current work we consider only the material aspects that would influence the chemistry, so this (4×4) surface area suffices.

The atomic positions on both sides of the ideal slab model are minimized to equilibrium positions. The bottom two tri-layers on the back-side of the relaxed slab are frozen to this clean surface structure in every slab simulation. The metal clusters and surface defects are applied to the front-side surface side of the slab. Significant surface relaxations, and relaxations around defects, are observed to extend one tri-layer from a site. We consider defects (vacancies) in the second tri-layer, mandating a minimum of five tri-layers be included for an acceptable slab model.

The local moment countercharge (LMCC) method[51] is used to eliminate spurious slab surface dipole fields that might be generated from modeling adsorption on a single side of the slab. The vacuum spacing between slabs is made wide enough to ensure that atomic orbitals do not impinge on the vacuum edge (this condition is explicitly enforced through automated tests in every calculation). This isolates a slab from its periodic images both electronically and electrostatically, tantamount to a strictly two-dimensional calculation. A generalized LMCC method is used to impose the correct electrostatic boundary conditions to enable accurate calculations of defects with net charge in the bulk and the surface.[52, 53]

Chemical reference systems

The Ni/CeO_2 chemical system is comprised of components that are particularly vexing for DFT methods. It is not the intent of this work to fully resolve these issues; but the need to establish the underlying merits of the approach mandate that an accounting be presented of how the current methods perform in with regard to these issues.

Cerium, in particular, is a problem, the easily mutable oxidation state already injecting itself into struggles to describe the elemental fcc metal correctly.[54, 55, 56, 57, 58] The non-magnetic ground state α-fcc structure is best described as a Ce^{IV} with no $4f$ occupation, while the magnetic γ-fcc has a larger lattice parameter best described as a Ce^{III} with a $4f^1$ occupation. Foreshadowing similar issues in CeO_2 and Ce_2O_3, it was found that smaller-U were needed to properly describe the relative stabilities and the structures, while larger-U gave better descriptions of the electron structure.[58] The computed PBE lattice constants for the α-fcc phase, reported to be 4.72 Å[56] and 4.74 Å,[57, 58] are an anomalous (for GGA) and severe underestimate of the 4.85 Å experimental lattice constant, that a $+U$ treatment did little to remedy.[58] Our Ce^{IV} atom, having excluded a $4f$-occupation, yields a PBE lattice constant of 4.96 Å for fcc Ce. This result is 2.3% larger than experiment, an overestimate consistent with the usual performance of the GGA approximation.

Our CeO_2 PBE lattice constant is computed to be 5.534 Å, with B=191 GPa. This equilibrium lattice constant is imposed in all the simulations in this study. This $4f$-less Ce lattice constant is again larger than other PBE results.[31] The bulk modulus is also larger, which better approaches the experiment $B = 220(9)$ GPa.[59] The 2.7% overestimate of the experimental lattice constant 5.391 Å (the 0K value as extrapolated by Castleton, *et al.*[60]) is again reasonable, within GGA expectations. The computed formation enthalpy of CeO_2 (*cf.* α-Ce(fcc) and the triplet O_2 molecule) is -9.80 eV, which despite the very different construction of the Ce atom, is in general agreement with previous GGA and GGA+U results.[32, 57, 61, 62]

The Ce atom gives a satisfactory description of the structure and energetics of CeO_2, as good as—in some respects better than—U-modified GGA methods. The crucial aspect is that the absence of Ce $4f$-functions has pushed the unoccupied $4f$-derived levels higher in the Kohn-Sham (KS) gap. Without the Ce $4f$ basis functions, the usually problematic $4f$ state is shifted to much higher, expanding the effective gap in CeO_2 to 3.7 eV. This imposition of a Ce^{IV} oxidation state proves sufficient to avoid the unphysical delocalization of an oxygen vacancy state into Ce $4f$ orbitals.

The oxygen molecule is the conventional experimental standard reference state for oxygen. As Pacchioni pointed out,[36] the use of half the energy of the ground state O_2 molecule as the chemical reference state, $\mu(O;O_2)$, is rather awkward in computational studies. Awkward both in term of accuracy—because DFT inaccurately describes the binding of O_2 molecule–and awkward in terms of usefulness in comparing the results of different computational studies—different DFT methods exhibit very different errors for O_2. To avoid these difficulties, Lutfalla, *et al.*,[32] advocated using a dehydrogenation of water, *i.e.*, a chemical potential $\mu(O;H_2O)$ defined by

$$\mu(O;H_2O) = E(H_2O) - E(H_2), \tag{2.2}$$

as the oxygen chemical reference energy in CeO_2 simulations. This definition "bypasses" the difficulties stemming from DFT inaccuracies in describing O_2.[37] Our computed difference between $\mu(O;O_2)$ and $\mu(O;H_2O)$ is -2.61 eV. This compares favorably to the experimental shift of -2.48 eV and matches exactly the O_2 to H_2O shift in plane wave GGA methods quoted by Paier.[37] While this oxygen reference state is formally arbitrary, it is more transferable (between different studies) to use the more computationally consistent hydrogenation reference, and, as we show later, more chemically insightful to use $\mu(O;H_2O)$. We use this reference in presenting our results in the following.

The Ni atom reference is similarly arbitrary, and similarly fraught. The Ni atomic ground state is a triplet d^8s^2. However, once more, DFT and solid state DFT implementations cannot give a proper description of this electronic configuration, introducing uncontrolled errors in comparison to experiment, and also making comparisons between different DFT studies difficult. In the calculations of Ni atom adsorption, we use the singlet-d^{10} Ni atom as our chemical reference. It still gives a meaningful measure of an atomic adsorption energy. A triplet-spin Ni atom is computed to be 0.80 eV lower, but we reiterate that this triplet energy is not physically reliable. It is provided here strictly to facilitate comparisons to other

studies that might use the triplet-Ni as a reference. To avoid the difficulties associated with a proper DFT description of the triplet ground state nickel atom, we recommend using the singlet-Ni—a clean d^{10} atom that can be properly represented in DFT—as the Ni chemical reference in computational studies.

Results

Nickel clusters on CeO_2(111)

A comprehensive exploration of the potential energy surface for a single Ni atom on the clean ceria(111) surface includes:

- Three atop sites: atop the Ce; above the O_{top} atom; and above the O_{sub} (also commonly labeled as the "hollow" site);
- Three bridge sites: between the Ce—O_{top}, between the O_{top}—O_{sub}, and between Ce—O_{sub} (commonly labeled as a"bridge" site,[15] as it bridges between two O_{top} sites);
- An off-symmetry site: within the triangle defined by the Ce, O_{top}, and O_{sub} sites.

We find a off-symmetry site, slightly displaced off the Ce—O_{sub} mirror plane, to be the lowest energy adsorption site for a single Ni atom on the ceria(111) surface, as illustrated in Figure 2.2. The atop-Ce and atop-O_{top} sites are maxima on this surface, clearly disfavored, at 2.12 and 0.69 eV, above the ground state position, respectively. The atop-O_{sub} site is 0.27 eV above the ground state. While the O_{sub} site is a minimum along the mirror plane between the top- and sublayer-oxygen, a nickel located atop the O_{sub} would slide down toward the nearest neighbor Ce atom to a Ce—O_{sub} bridge site that is 0.25 eV lower, and then relax further to its ultimate minimum another 17 meV lower just off that bridge site. This same off-symmetry site was reached relaxing from multiple sites within the triangle, clearly identifying this as the minimum energy adsorption site.

This Ni atom adsorption is in substantial agreement with Hahn, *et al.*,[15] who used a PBE+U approach in a local orbital code (including f-functions). They found the "bridge" site (bridging between two O_{top}) to be the lowest energy adsorption site, 0.19 eV below the "hollow" site (atop O_{sub}). That they did not find our off-bridge distortion might be due to their only sampling high-symmetry (atop and bridge) configurations. We note that our result indicates that this Ni adsorption structure is insensitive the use—or absence—of a $+U$, and to the presence—or lack—of $4f$-functions.

Other results using PBE+U, by Lu, *et al.*,[14] Carrasco, *et al.*,[21] and Riley, *et al.*,[16] instead find the atop-O_{sub} site to be favored. Hahn reports an Ni adsorption energy of -2.18 in the O_{sub} site, these others authors report -1.51, -3.68, and -3.24 eV, respectively. That the Lu result is an apparent extreme outlier is due to their use of a free-standing (2×2) Ni

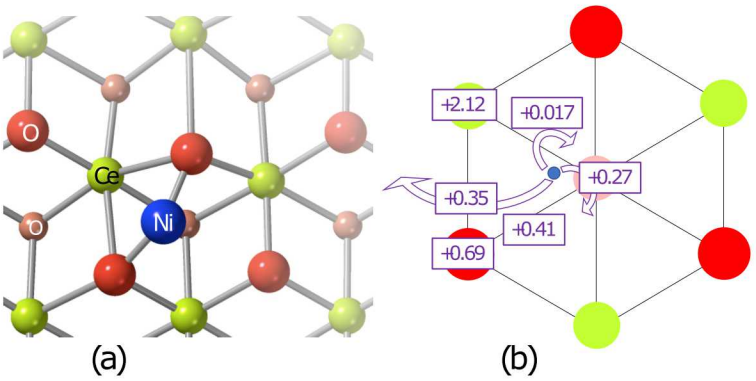

Figure 2.2. Adsorbed Ni atom on $CeO_2(111)$ surface. (a) Diagram of optimal surface adsorption site, in a position offset from the O_{sub}—Ce line, bridging between two O_{top} sites. (b) Schematic depicting energies at high-symmetry Ni adsorption sites, and migration barrier energies (with respect to the minimum energy structure, in eV). The barrier across the O_{sub}—O_{top} line is not through the mid-line saddle point (+0.41 eV), but instead is over the O_{sub} site (+0.27 eV).

layer as their Ni reference energy (they did not quote an Ni atomic energy), while the others all used a (triplet) gas phase Ni^0 atom as their reference energy.

Using the same functional (PBE) and similar U-values, these other authors nonetheless quote rather different values for the nickel atom adsorption. This might be attributed to the practice and problem dependence observed in an $+U$ approach[35, 42, 63] that can lead to variations in nominal defect formation energies as large as 3 eV,[42] but it is also possible that this is a problem in establishing a consistent Ni atomic reference with the triplet-Ni atom.

Our adsorption energy of a single Ni atom in the off-symmetry ground state structure, using the less problematic singlet-d^{10} Ni atom reference, is -3.13 eV. To compare directly to these previous results, we obtain -2.86 eV binding of a singlet-d^{10} Ni atom at the O_{sub} site. This translates to -2.08 eV with respect to the problematic triplet-Ni atom reference, in good agreement with -2.18 V binding obtained by Hahn.[15]

This Ni reference energy is, repeating, formally arbitrary, useful mostly to facillitate meaningful quantitative comparisons and benchmarks between different studies. The important aspect, for the purpose of understanding the adsorption kinetics, is that a Ni atom adsorbs strongly on the surface, so strongly that it will not desorb again at any temperature of interest.

In particular, the Ni desorption energy is much larger than its migration energy on the surface. Figure 2.2 summarizes the critical points on the potential energy surface important

to migration. To traverse the Ce—O_{sub} edge into the neighboring channel, only 17 meV is required. The O_{top}–O_{sub} edge has a saddle point at 0.41 eV, but the lowest-energy crossing across that edge into the neighboring channel is actually right at the O_{sub} site. For long range migration, the overall barrier is the highest-energy crossing of the three edges of the channel triangle (otherwise the Ni atom would locally orbit a single site). The saddle point through the Ce—O_{top} edge is 0.35 eV above the ground state site, and this constitutes the overall surface migration barrier.

The diffusion along the surface, therefore, has a computed activation energy of <0.4 eV, indicating facile migration of a single adsorbed nickel atom on the $CeO_2(111)$ surface even at room temperature. Such a low surface migration barrier suggests that individual Ni atoms will diffuse rapidly along the surface until they find some deeper sink, *e.g.*, a defect or a step edge that might bind the Ni more strongly, or encounter other adsorbed Ni atoms to bind into clusters that are less mobile. This notion is consistent with (note: not proven by) experiments that have not, to date, observed single adsorbed Ni atoms at the ceria surface. For 0.1 monolayers of nickel deposited on a ceria surface at 300K, Liu, *et al.*,[8] observed Ni clusters, but reported no isolated Ni atoms on their surface that might indicate an immobile adsorbed nickel atom.

Two adsorbed nickel atoms form an adsorbed dimer, bound by 0.65 eV with respect to separated adsorbed atoms. We note that for simplicity in this case and in the following, results of spin-singlet (no spin) calculations are quoted; the effects of spin-polarization will be discussed afterwards, and do not materially affect the analysis.

As shown in Figure 2.3, the two Ni atoms bridge asymmetrically across a pair of O_{top} sites. Figure 2.3(a) shows a conventional ball-and-stick model of this structure, Figure 2.3(b) depicts a more abstracted form focussed on the surface positions of the Ni atoms that proves more useful for illustrating the structures of larger clusters. Included in the Supplemental Information is a detailed listing of the entire series of adsorbed Ni cluster configurations.

An extensive search for the ground state structure reveals a rather flat PES with multiple shallow minima, suggestive of a dimer that is also mobile.

A trimer is more strongly bound. A dimer captures a third adsorbed Ni, with an energy gain of 1.52 eV. The trimer adopts a triangular structure that slots into a triangular "socket" defined by three O_{top}. There are two distinct such sockets on the surface, one centered on the Ce atom, the other centered above the O_{sub} atom, as shown in Figure 2.4. These have binding energies within 30 meV of each other, equivalent within any credible numerical resolution that can be claimed of the calculation. The Ce-centered trimer retains the full C_{3v} symmetry, while the O_{sub}-centered trimer is slightly (51 meV) distorted (twisted) from a three-fold symmetric configuration. This result reveals two important structural motifs of Ni clusters on ceria(111): first, a strong, but somewhat adirectional bonding of the nickel atoms to a single surface oxygen that fastens the cluster to the surface; second, a triangular packing that maximizes coordination between nickel atoms, akin to the close-packing in bulk *fcc*-Ni.

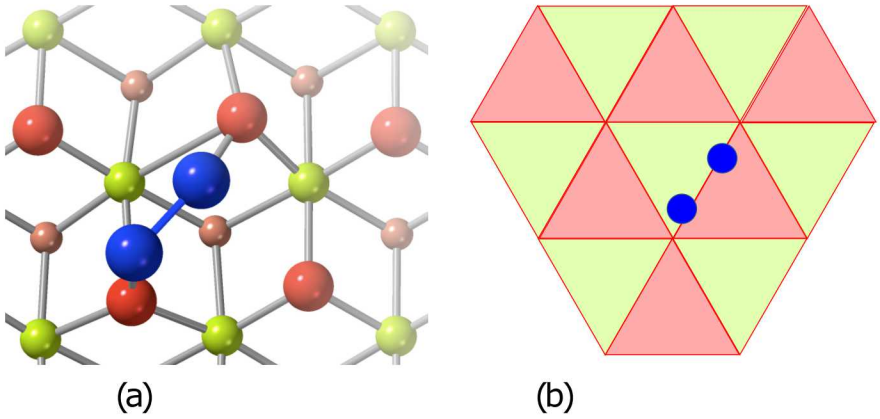

Figure 2.3. Adsorption geometry for the adsorbed Ni dimer ground state structure. (a) Ball-and-stick diagram showing the nickel atoms (large blue balls) bridging asymmetrically between two O_{top} (red) atoms. (b) A stylized representation of the structure, the CeO_2 substrate depicted using the triangular lattice defined by the top oxygen atoms, with pink triangles above the subsurface oxygen and the chartreuse triangles centered on the Ce atoms.

The binding of a fourth Ni atom to this trimer is stronger yet. Confined to the single surface layer, a new Ni atom is bound to the edge of the trimer to form a rhombus by 1.46 eV. However, it is more stable for the cluster to be a Ni tetrahedron. The O_{sub}-centered tetrahedron yields a a total attachment energy of 1.72 eV. The Ce-centered tetrahedron is less favorable, at 1.57 eV attachment energy. The barrier to climb from the flat rhombus to the O_{sub} centered tetrahedron is only 0.71 eV (a corner atom folds over the step) and to the Ce-centered tetrahedron is 0.87 eV (via a concerted process where the rhombus corner pushes an edge atom to the peak). The two-level tetrahedron will readily form upon the capture of a fourth nickel atom.

This single-atom attachment energy, stemming from this surface reaction $Ni_{(n-1)}$/ceria + Ni_1/ceria $\rightarrow$ Ni_n/ceria:

$$E_{attach}(n) = E(Ni_n/ceria(111)) - E(Ni_{(n-1)}/ceria(111)) - (E(Ni_1/ceria(111)) - E_{ceria(111)}), \quad (2.3)$$

first proposed (in the context of Ni/ceria) by Riley, *et al.*,[16] proves particularly illuminating in understanding the stability of different N cluster sizes.

The four-atom Ni cluster is found to be a magic cluster. A fifth Ni atom attaches to the edge of tetrahedron, with a reduced attachment energy of 1.33 eV. The over-Ce tetrahedron is favored over the over-O_{sub} tetrahedron, reversing the four-atom tetrahedrom site order. The difference between these five-atom clusters is only 0.06 eV, however, and the second-layer Ni atom hops between the sites with a very small barrier.

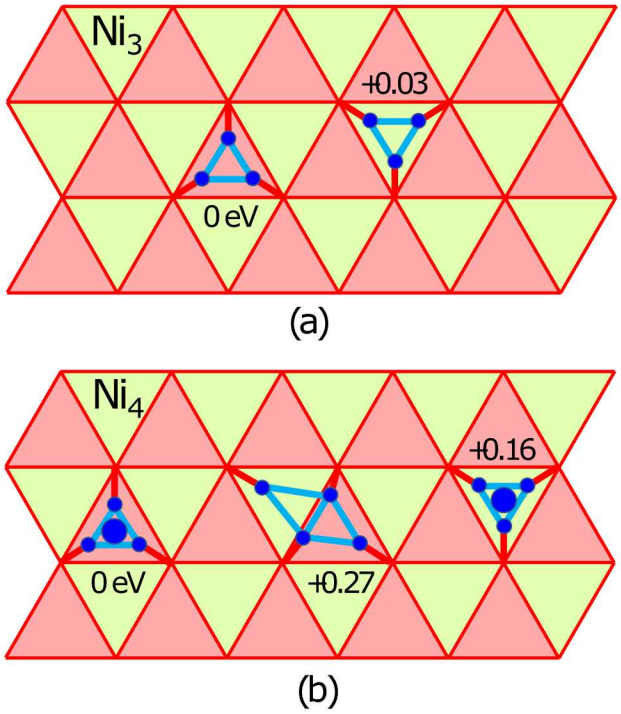

Figure 2.4. Low energy adsorption configurations for absorbed Ni trimers and tetramers. (a) Ni trimer adopts a triangular shape that fits into triangles of O_{top}, favoring the O_{sub} just slightly over the Ce site. (b) Ni tetramer can attach another edge Ni to form a single layer rhombus, but prefers (with modest barriers) to climb atop the triangle to form a tetrahedron, favoring the O_{sub} more strongly.

This cluster binds a sixth Ni atom with only 1.23 eV (one atom atop a five-atom trapezoid, adding another atom to the base rhombus layer), a seventh with 1.41 eV (a second atom atop a five-atom trapezoid), and an eighth attaches with 1.23 eV (squeezing yet a third atom into a triangle atop the trapezoid). This sequence appears to attempting to maximize coordination within the cluster of adsorbed nickel atoms, in a close-packed arrangement.

The nine-atom cluster switches motifs. The base layer transforms to a seven-atom hexagon embedded into a larger O_{top} hexagon on the surface. The central Ni in this hexagon binds atop the central O_{top}, and the outer hexagon Ni bond to one of the outer hexagonal O_{top}. The two atoms in the second layer position themselves into Ni-bridging sites, a structure also reported by Hahn, *et al.*[15] The attachment energy accompanying this rearrangement increases to 1.74 eV, rivaling the Ni_4 cluster attachment energy.

The 10-atom cluster completes a triangle on the second layer topping this hexagon, and is seen to mark another magic cluster size. This close-packed structure gives a Ni attachment energy of 1.88 eV.

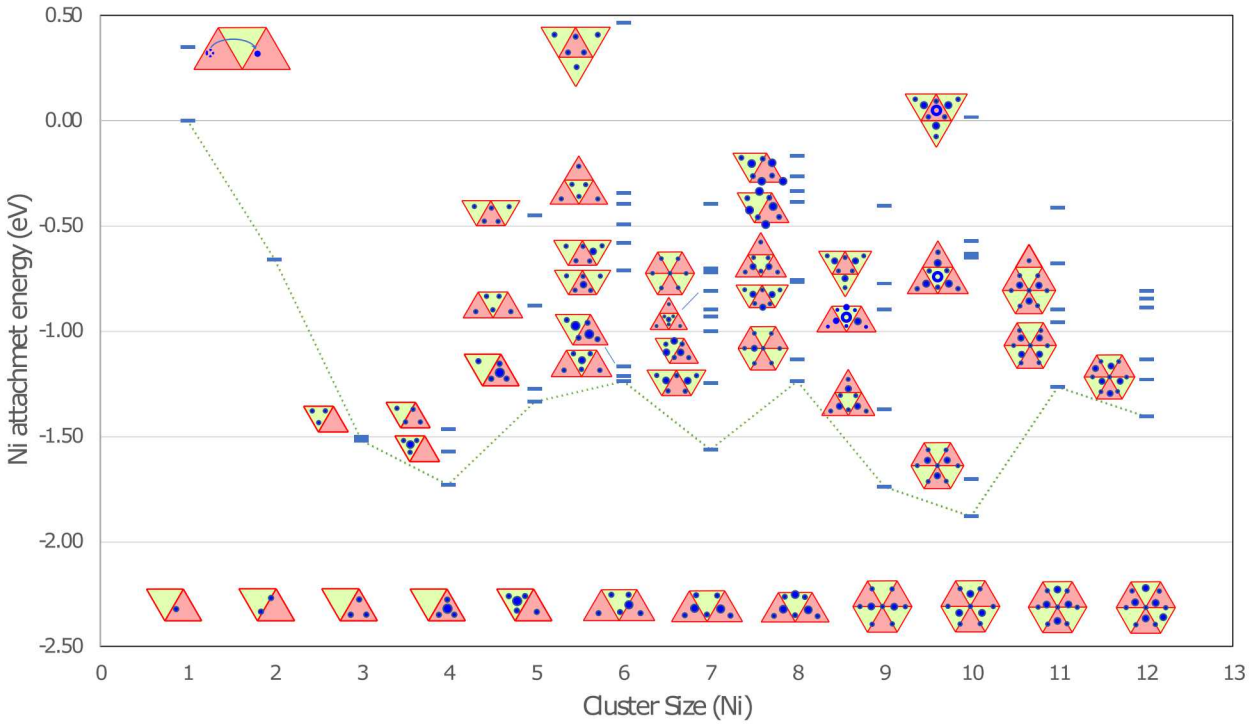

Figure 2.5. Nickel atom attachment energy of Ni clusters on ceria(111) Note that a complete detachment must additionally overcome a Ni_1 diffusion energy (0.35 eV) to escape the cluster. The optimal clusters tend to be bilayered, with close-packed (triangular or hexagonal) base layer with close-packed layers above it. The Ni_4 and Ni_{10} clusters exactly satisfy these conditions, and are most stable against detaching an atom.

Additional attachments on the outside of the hexagon base puts new Ni atoms too far from a O_{sub} to form as favorable a bond. The best attachment of an eighth atom at the edge of the based hexagon layer yields at best ~0.9 eV. Additional atoms instead climb onto the base hexagon to join the second layer. This requires compromises in the close-packed coordination of the cluster. The 11-atom attachment energy is only 1.26 eV and the 12-atom only 1.32 eV. It is energetically favorable for the cluster to continue to accrete diffusing Ni atoms, but the additional Ni attachment energy is much less than that of the 10-atom magic cluster.

The attachment energy as a function of cluster size, $E_{attach}(n)$ *vs.* Ni_n, is illustrated in Figure 2.5. It can clearly be seen that a four-atom and a ten-atom cluster close what appear to be particularly stable shells in a magic number cluster.

The inclusion of spin polarization does not impact these results meaningfully. The adsorbed Ni_1 is only stable as a spin-singlet (and our attempts to converge a spin-triplet $Ni_1[2+]$

failed). A spin-triplet is the ground state for Ni_x, for $x = 2 - 5$, with a spin polarization energy of 0.3-0.6 eV, with the magic $x = 3, 4$ clusters gaining more that the others. For the Ni_{10}, the spin-triplet gains 0.25 eV over a spin-singlet, but the ground state has six majority electrons that is 0.53 eV more stable than the singlet. The overall magnetization, $0.6\mu_B$/Ni, perhaps coincidentally, matches that of bulk Ni, although the net magnetization energy is slightly larger than computed for bulk Ni.[48] Overall, the shape of the attachment energy with cluster size remains the same with spin included. While the facile creation of open-shell d-electrons undoubtably facilitates the catalytic activity of the nickel clusters, the energies involved in magnetization remain modest.

Oxygen vacancies - bulk ceria

Before proceeding to a discussion of oxygen vacancies at the ceria surface, it behooves one to consider the limiting case of an oxygen vacancy in bulk ceria.

The conventional objection to the use of standard first-principles density functionals in ceria, and particularly as applied to reduced surfaces, is the metallic delocalization of the electrons within an oxygen vacancy using LDA or GGA, deemed a "*complete* failure of the GGA approximation" (emphasis in source).[35] This failure, due to a delocalized occupation of $4f$-states on the cerium atoms in the CeO_2 lattice, is used to motivate—and justify—the use of an empirical $+U$ approach, despite this itself being deemed "unsatisfactory".[35]

The excluded $4f$-basis approach prevents this delocalization. The neutral bulk oxygen vacancy has a well-defined defect state inside the Kohn-Sham gap, occupied by two electrons that are Coulombically bound by a Madelung potential at the vacated oxygen site. Using $\mu(O;H_2O)$, the formation energy of the neutral vacancy is found to be 3.214 eV in the smallest (96-site) supercell, 3.207 eV in the 324-site supercell, and 3.202 eV in the largest 768-site supercell. We quote three decimal places above, finer than any credible numerical uncertainty, only to resolve a distinction between the different supercells. Add 2.61 eV to these values convert to the conventional, but computationally less reliable triplet-O_2 standard reference state. Reflecting the large band gap and the strong localization in the computed defect state, this formation energy of $v_O[0]$ is already well converged in the smallest supercell. This, incidentally, also verifies the convergence of the k-grids used in these supercells.

Computed bulk $v_O[0]$ formation energies in the literature, even restricted to just GGA functionals (although with occasionally differing U values),[40, 61, 62, 64, 65, 66, 67] span a wide range of 4 eV,[35] precluding any meaningful quantitative benchmark comparisons. The current calculations give a formation energy for the neutral oxygen vacancy at the high end of this range, slightly above the 4-5 eV heat of reduction per oxygen atom reported in experiments.[68]

The computed migration barrier for the bulk neutral neutral vacancy is 1.67 eV. A nearest neighbor oxygen along a (001)-axis squeezes between the two Ce atoms of the shared edge of the tetrahedra around the two oxygen site. This stands in contrast to literature using

DFT+U methods, which after creating a pair of Ce^{III} to accompany the oxygen vacancy, yield 0.5-0.6 eV barriers vacancy diffusion.[66, 67, 69, 70, 71, 72] This unusual consistency among different $+U$ calculations for the diffusion barrier is in agreement with diffusion energies ($\sim$0.5 eV) inferred from ionic conductivity experiments in doped ceria.[73, 74]

The neutral vacancy has a doubly occupied defect state in the Kohn-Sham eigenvalue gap, 2.7 eV above the valence band edge. This state can be ionized once to create a $v_O[1+]$ state, the nearest neighbor Ce atom shifts from a slight (0.6%) inwards position in the $v_O[0]$, to sit outwards by 3.7%. A second ionization, 0.07 eV deeper, creates the $v_O[2+]$ defect. The nearest neighbor Ce now sits 8.1% outwards. Jiang, *et al.*, using first-principles PBE, had predicted a $-U$ $v_O(0/2+)$ transition at +1.9 eV above the valence band edge, the (0/1+) transition at 1.5 eV being deeper than the (2+/1+) transition. The current results resemble more the PBE+U results from Zacherle, *et al.*,[62] which had the (0/1+) transition 0.12 eV above the (1+/2+) transition, in the standard order, for the undecorated oxygen vacancy. When they included a pair of U-induced Ce^{III} atoms into the vacancy description, this overall system had a $-U$ (2+/0) transition from the simple $v_O[2+]$ vacancy to the neutral $(2Ce^{III} + v_O)[0]$ at 1.53 eV.

The charged state calculations use a local moment countercharge method[52, 53] that give accurate descriptions of charge transition energies.[75] The extrapolation to infinitely dilute defect densities uses a Jost screening model[53] with a static dielectric constant of 25 as computed with DFT[72] (and an unpolarized skin depth of 2.0 Bohr[53]). The accuracy of the method is verified through consistency (within 0.02 eV) of defect transitions computed in independent extrapolations from the different 96-, 324-, and 768-site supercells.

The calculated migration barrier for the $v_O[2+]$ is 0.45 eV. That this [2+] barrier is much smaller than the barrier for the neutral vacancy is to be expected: a O[0] atom is much smaller than a O[2-] ion, and therefore will squeeze between the two Ce atoms at the barrier more readily. This migration barrier of the simple vacancy, in its [2+] charge state, matches the $+U$ barriers for the *neutral* v_O. This [2+] migration barrier is now in excellent agreement with the experimental estimates. The experimental analysis[74] specifically extracted the diffusivity of charged free vacancies de-associated from their compensating dopant defects. This analysis suggests that the crucial aspect for explaining the bulk vacancy diffusion experiments is the presence of $v_O[2+]$. The creation of nearby compensating Ce^{III}—if such species are created—is only incidental, not fundamental to v_O diffusion.

Oxygen vacancies - ceria(111) surface

The potential importance of oxygen vacancy formation and transport at the ceria surface has long been appreciated as a crucial element of understanding the redox behavior in ceria. Calculations of ceria(111) surface vacancies date back to at least 2004, when Yang, *et al.*,[40] discovered that a local GGA functional, just as for the bulk vacancy, created an unphysical metallic ground state with a fully delocalized pair of electrons. Nolan, *et al.*,[76] and Fabris, *et al.*,[42] soon eliminated this delocalization with the use of GGA+U methods to stabilize the

Table 2.1. Computed values from literature for the oxygen vacancy formation energy (in eV) at the ceria(111) surface, in an O-rich limit using the triplet-O_2 as the standard reference.

Functional	Slab model/k-grid	$E_f(\ v_O^{top}\ )$	$E_f(\ v_O^{sub}\ )$
PBE+U(4.5)[a]	$(2\times2)\times3L$ / 3^2	2.34	1.87
HSE[a]	$(2\times2)\times3L$ / 2^2	3.10	2.65
PW91+U(5.0)[b]	$(4\times4)\times4L$ / 2^2	2.23	2.17
(GGA)+U(5.0)[c]	$(3\times4)\times3L$ / Γ	2.11	1.94
PBE+U(4.5)[d]	$(4\times4)\times4L$ / Γ	1.93	1.76
PW91+U(5.0)[e]	$(3\times3)\times4L$ / 2^2	2.18	1.81
PBE+U(4.5)[f]	$(6\times6)\times6L$ / Γ	3.29	3.23
PBE+U(4.5)[g]	$(4\times4)\times4L$ / Γ	2.38	2.04
PBE+U(5.0)[h]	$(4\times4)\times4L$ / Γ	1.94	1.72

(a) Ganduglia-Pirovano, *et al.*, 2009.[77]
(b) Zhang, *et al.*, 2009.[78]
(c) Li, *et al.*, 2009;[79] specific GGA functional not documented, likely PW91.[80]
(d) Murgida, *et al.*, 2013.[81]
(e) Plata, *et al.*, 2013;[82] also including a $+U$=5.0 eV on the O-2p.
(f) Hahn, *et al.*, 2015;[15] using a local-orbital method.
(g) Su, *et al.*, 2016.[83]
(h) Zhang, *et al.*, 2019.[84]

vacancy electrons into reduced Ce^{III} atoms. Echoing the considerable variation reported in the formation energy of bulk oxygen vacancies (see above), these early results (summarized in an early review[35]) showed multi-eV variations in vacancies at the surface, stemming from differences in formulation of $+U$, supercell surface area, slab thickness, location of the reduced Ce^{III} ions.[42]

Studies since have largely coalesced around a consensus computational model ($U\sim$5 eV), and yielded more consistent results for v_O at ceria(111), as recounted in Table 2.1. Confirming the early first-principles-GGA prediction that the vacancy at the subsurface site, v_O^{sub}, would be more stable than the vacancy at the top O site, v_O^{top},[40] these GGA+U results all find the subsurface vacancy more stable, by 0.2-0.5 eV. The formation energy, $E_f(v_O^{sub})$ given by the GGA+U were seen to be quite small, only 1.8-2.2 eV. The HSE prediction, one alternative to a $DFT+U$ approach, gives a slightly larger formation energy.[77]

Just as for the bulk vacancy, our PBE calculations that preclude $4f$-occupation on the Ce result in localized surface oxygen vacancy states. The Kohn-Sham level for the defect state

Table 2.2. Computed neutral oxygen formation energies (in eV)[a] for 5 tri-layer ($5L$) slabs, as a function of depth into the slab, using an O-rich $\mu(O;H_2O)$ reference. (As noted in Section 2, the O_2-based PBE reference leads to values 2.61 eV higher).

Unit cell/k-grid	v_O^{top}	v_O^{sub}	v_O^{L2+}	v_O^{L2-}
(2×2) / 2^2	3.250	2.985	2.880	3.262
(2×2) / 3^2	3.252	2.956	2.867	3.254
(3×3) / 2^2	3.326	2.961	2.873	3.255
(4×4) / Γ	3.226	2.946	2.875	3.252
(4×4) / 2^2	3.248	2.944	2.860	3.249
(5×5) / Γ	3.260	2.941	2.870	3.252
(6×6) / Γ	3.250	2.942	2.871	3.250

(a) Three decimal place shown only to discern differences between slabs; results have ± 0.01 eV numerical uncertainties

does climb in the KS gap with respect to the bulk analog, but the vacancy state remains in the gap, localized in the Coulombically-stabilized site vacated by the oxygen atom.

Our computed neutral oxygen vacancy formation energies are presented in Table 2.2. To investigate the effects of supercell size, the calculations are repeated from (2×2) through (6×6) unit cells, with varying k-point sampling in the surface BZ. Also, leveraging the latitude granted by using thicker $5L$ slabs, the stability of a vacancy into the second tri-layer is investigated.

The results for the neutral vacancy are well converged with (4×4) unit cells and larger, to within $\sim$10 meV. The smaller supercells are still satisfactory, provided a beyond-Γ k-grid is used. In accord with the GGA+U studies cited above, the subsurface vacancy is more stable than the top vacancy, here 0.3 eV lower. However, a vacancy in the next deeper layer, v_O^{L2+}, is lower yet, by another 0.07 eV. The vacancy in the fourth layer of oxygens, v_O^{L2-} returns to the the same energy as v_O^{top}.

The vacancy calculations extending to a $9L$ slab in the (4×4) / Γ unit cell give results within 0.01 eV of the $5L$ slab. Using this thicker slab, Figure 2.6 plots $E_f[v_O]$ for vacancies eight oxygen layers deep (through the fourth tri-layer). These results indicate that any (neutral) oxygen vacancies near the surface will collect in the *two* subsurface layers, leaving the topmost layer of oxygen atoms in place. The vacancy energy achieves the asymptotic bulk limit after the third tri-layer.

Our computed migration barrier from v_O^{top} to v_O^{sub} is 0.66 eV (the barrier to return is 0.94 eV), from v_O^{sub} to the next sublayer is 0.81 eV (0.88 eV to return), and down further

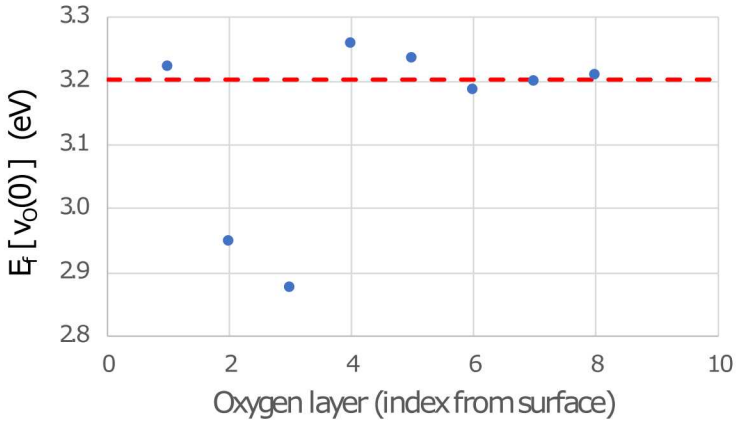

Figure 2.6. Formation energy (in eV) of a neutral oxygen vacancy at the ceria(111) surface, as a function of depth into the substrate, using the H_2O-derived O reference energy $\mu(O;H_2O)$. Dashed line indicates the computed asymptotic bulk value.

into the fourth layer of oxygen atoms is 1.84 eV. Compared to the bulk barrier (1.67 eV), the barriers to vacancy migration between the top three oxygen layers is much smaller. Proximity to the surface strongly facilitates vacancy motion.

The potential energy surface for the $v_O[2+]$ at the $CeO_2(111)$ surface changes. The $v_O[2+]$ prefers the top two layers, with the sublayer slightly favored (by 0.15 eV in the $(4 \times 4) \times 5L$ slab). The next sublayer, the lowest energy site for the $v_O[0]$, is instead $\gtrsim$0.5 eV higher, and the next layer deeper is yet another 0.5 eV less stable. The $v_O[2+]$ induces larger local lattice distortions that the neutral and induces long-range screening, so that the ionized defect is less well converged with slab model size. Extending to $9L$ or expanding to a (6×6) unit cell reduces the margin favoring the sublayer to only $\sim$0.07 eV, while lowering both top layers with respect to the deeper layers by another 0.1 eV. Despite gaining additional screening energy as the net charge descends into the bulk, the $v_O[2+]$ is mostly confined to the top two layers.

Just as in the bulk, these results for the undecorated, simple $v_O[2+]$ mimic the GGA+U literature results for $v_O[0]$ in Table 2.1, where the v_O was decorated with two U-induced Ce^{III}.

The diffusion of oxygen vacancies is the mechanism behind oxygen transport in ceria, and has motivated studies of vacancy migration at the ceria(111) surface using GGA+U. Li, *et al.*,[80] favoring the sublayer by 0.17 eV, gave a 0.44 eV migration barrier from the top layer into the sublayer. Plata, *et al.*,[82] exploring different sites for the associated Ce^{III} sites around the vacancy, determined a barrier as small as 0.17 eV to the sublayer site (with 0.37 eV lower energy). Likewise, invoking concerted motion of the associated small polaron (Ce^{III}), Su, *et al.*,[83] also came to a small 0.15 eV barrier to their 0.34 eV deeper sublayer

vacancy. Zhang, *et al.*,[84] identified barriers as small as 0.06 eV from DFT molecular dynamics trajectories.

Our computed barrier for the simple v_O[2+] migration into the sublayer is only 11 meV, for the $(4 \times 4) \times 5L$ slab. This small barrier, once again, essentially echoes the result from the GGA+U neutral ($v_O + 2\mathrm{Ce}^{\mathrm{III}}$). The slightly higher barriers in the literature GGA+U studies likely can be attributed to the lattice distortions being confined into thinner slabs and smaller unit cells. The more extended, expanded slabs used here better accommodate the greater distortions in the (charged) defects.

There is no direct experimental measurement of migration barriers for the vacancy at the surface. Such data would be highly valuable.

Analysis and discussion

What is known, from the observations of Namai, *et al.*,[85] using atomic force microscopy, and from Esch, *et al.*,[43] and from Grinter, *et al.*[86], using scanning tunneling microscopy (STM), is that isolated single vacancies at the ceria surface are immobile at room temperature. Esch, *et al.* reported that they did not observe diffusion of vacancies at the surface until temperatures higher than 400°C. The low barriers predicted within a GGA+U picture of a $\mathrm{Ce}^{\mathrm{III}}$-decorated v_O (and also the analogous depiction of the surface vacancies as simple v_O[2+]) are contradicted by these observations. With GGA+U migration barriers $\lesssim$0.2 eV, vacancies would exhibit rapid diffusion even below room temperature; these (high-temperature) STM observations of localized vacancies would be impossible.[87] Furthermore, the redox activity of the ceria support is known to activate at elevated temperatures,[65] which, stipulating that vacancy motion is integral to this redox behavior, also indicates much larger barriers to vacancy motion at ceria(111).

The simple v_O[0] picture given by the current results, with barriers $\gtrsim$0.8 eV, is more compatible with the high-temperature STM observations and redox behavior. This simple-vacancy model also more naturally explains the three-fold symmetry observed in these AFM[85, 88] and STM[43, 86] experiments. A GGA+U-inspired $\mathrm{Ce}^{\mathrm{III}}$-decorated v_O model predicts broken symmetry structures, that requires the assumption of spatial averaging to regain the observed symmetry.[87]

The thermochemistry is also better represented by the simple-vacancy picture, which becomes apparent when one calibrates the vacancy formation energies using the H_2O-based oxygen chemical reference. The shift in the oxygen reference energy from a O_2- to H_2O-reference for plane wave GGA methods quoted by Paier [37] is 2.61 eV. The GGA+U vacancy formation energies listed in Table 2.1, at $\lesssim$2.0 eV) using an O_2-reference, then become $\lesssim -0.6$ eV in the hydrogenation reference. The implications become evident in writing the chemical reaction reducing the surface corresponding to this reference:

$$\mathrm{CeO_2}(111) + \mathrm{H_2(g)} \rightarrow \mathrm{CeO_2}(111){:}v_O + \mathrm{H_2O(g)}. \tag{2.4}$$

In the presence of H_2, removal of an oxygen atom from the GGA+U ceria surface (creating

an oxygen vacancy) to form water is *exothermic*. The ceria surface has been of great interest because of its active catalysis for hydrogenation reactions, *e.g.*, alkynes,[89] prompting studies to understand adsorption and activation of H_2 on ceria.[90] The re-referencing reveals that a ceria surface, with GGA+U, will not catalyze H_2 reactions, it will instead spontaneously be reduced.

The current results for the simple vacancy, without reduced-Ce^{III}, are better comparisons to the bulk vacancy formation energy, and the results of calculations (depicted in Figure 2.6 clearly demonstrate that the near-surface vacancies have comparable formation energies (which they must) that quickly converge to the bulk vacancy energy with depth. The conventional GGA+U oxygen vacancies, that spawn two reduced Ce^{III} satellites, are 2-3 eV too stable.

This failure of GGA+U to describe chemistry at the surface had been noted previously, for the description of CO on ceria(111),[63] who determined that a much smaller U = 2 eV—insufficient to spawn Ce^{III}—was needed to get the correct adsorption energetics. This unphysical bias toward reduced-Ce^{III} in GGA+U might have been anticipated from the error in heat of reduction of CeO_2 to Ce_2O_3, which is much too favorable with a $U\sim$5 eV,[31, 91] the reduction of Ce^{IV} to Ce^{III} overly favored by almost 2 eV.[32] To reproduce the bulk heat of reduction, requires a $U = 2$ eV. To reproduce the bulk heat of reduction, requires a $U = 2$ eV. Needed to obtain quantitatively reasonable thermochemistry at the surface, using this smaller U for an oxygen vacancy prevents delocalization into (*i.e.*. occupation of) the Ce $4f$ orbital, but does not engender reduced Ce^{III} neighbors.

The picture that emerges for oxygen vacancies at the ceria(111) surface is illustrated in Figure 2.7, which indicates an entirely new mechanism for oxygen transport at the surface. The neutral oxygen vacancies tend to segregate into the two sublayers. At high temperatures, the vacancies can traverse through this subsurface reservoir, with computed barriers $\lesssim$0.9 eV. Vacancies created at the top surface (perhaps fueling an oxidation reaction) can readily migrate into the this reservoir and, conversely, the top surface, being only 0.4 eV higher, is thermally accessible from a subsurface vacancy, to accommodate a reduction reaction at the surface. An interesting aspect of this mechanism is that the crucial transport processes can leave the top surface undisturbed. The stable oxide support retains its structural integrity in the midst of the flux of oxygen atoms at the surface necessary to enable the redox activity at the ceria(111) surface.

But then how does one reconcile the resulting model of neutral oxygen surface vacancies with the STM images showing structure compatible with (Ce^{III}-compensated) v_O[2+]?[85, 43, 92] The answer lies in the nature of the measurement: the STM is not measuring the clean undisturbed surface. The STM obtains its images through measurements of current, which, in an insulator like ceria, only occurs through the defects in the material, *i.e.*, the oxygen vacancy. The measurement itself removes electrons from the vacancy, changing the charge state from neutral to [2+], and induces the structural change that the STM then observes. That there potentially is a structural rearrangement indicative of such a change in charge prompted by the measurement would be consistent with an observation from AFM.[88] Their dissipative signal measured from the atoms above a subsurface vacancy exhibited significant

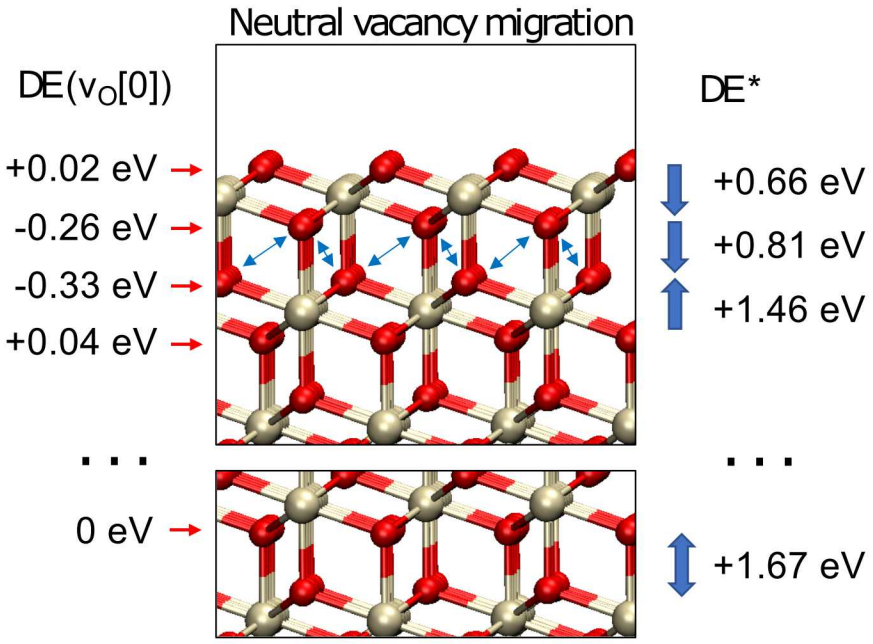

Figure 2.7. Energies and migration barrier energies (ΔE^*) of neutral oxygen vacancies near the $CeO_2(111)$ surface, referenced to the bulk values. The formation energies near the surface differ slightly from the bulk formation energy, but the migration barriers are much smaller near the surface. Neutral vacancies favor the two sublayers, and can diffuse laterally across the surface by interchanging between these two layers with barriers $\lesssim$0.9 eV.

(energetic and structural) relaxation in the course of a measurement.

That provides a consistent model for the essential oxygen transport function of the ceria support. Building upon this foundation, the results above for the Ni clusters upon this ceria support provide a model framework to understand the stability and activity of a dispersed metal catalyst.

A highly dispersed nickel catalyst is vital to maximize the interface perimeter between chemically active nickel clusters and bare ceria surface, and to avoid sintering into larger clusters that would lead to coking that deactivates the catalyst. The high mobility of the adsorbed Ni atom and the extra stability of magic cluster sizes, cognizant of the elevated temperatures needed to activate the catalytic behavior of the ceria-supported metal, provide the mechanisms that explain the dispersion of nickel clusters on ceria.[8]

Even at room temperature, individual nickel atoms on ceria(111) will be mobile. These mobile Ni combine to form clusters, which are more stable and less mobile. Judging from the binding energies alone, these clusters would grow indefinitely into a catalytically useless

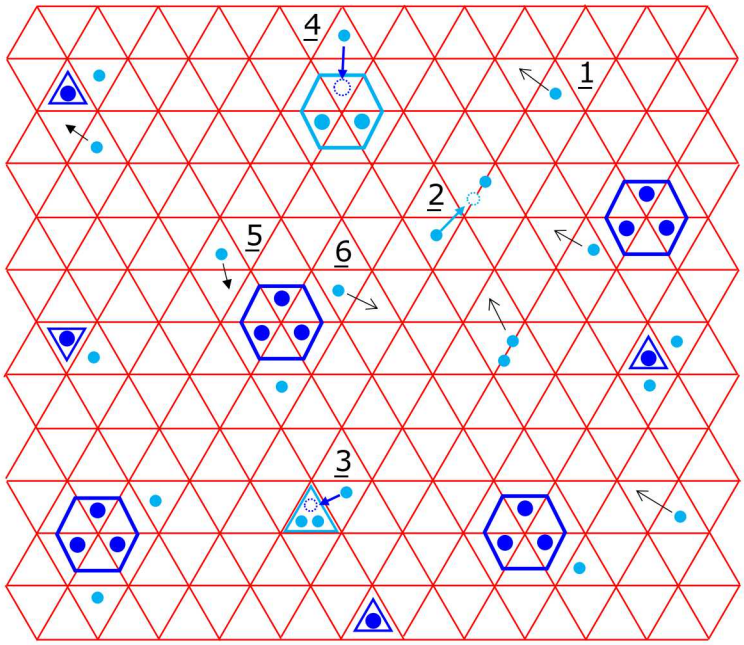

Figure 2.8. Illustration of hypothesized high-temperature Ni cluster ripening processes on the $CeO_2(111)$ surface around magic 4-atom tetrahedral (dark blue triangles) and 10-atom hexagonal (dark blue hexagons) clusters. Single Ni adsorbates **1** are highly mobile even at room temperature. Two Ni can combine to form dimers **2**, themselves transitory at low temperatures, unless a third Ni encounters the dimer first to form a pre-magic trimer **3**. A mobile Ni can also fill a shell on a magic cluster **4** to create a new stable surface species. Existing magic clusters will readily capture **5** a mobile atom (exothermic by >1eV). Being less well-bound than the magic clusters, these satellite atoms can detach **6** at elevated temperatures. The resulting surface consists of magic (filled-shell) clusters with associated satellite atoms, where those added atoms will intermittently be released onto the open surface of migrating single Ni atoms.

(sintered) mass. However, at elevated temperatures, such as those use to prepare and then use the metal-supported catalyst, the competing process of Ni detachment is potentially accessible. Magic clusters, those that ideally fit into O-bound chemical sockets on the ceria(111) surface and complete close-packed shells, are much more stable against detachment, as shown in Figure 2.5 for the Ni_4 and Ni_{10} clusters. Additional attached Ni atoms are not as strongly held, being less well able to bind to a surface oxygen.

The picture that emerges is illustrated in Figure 2.8, where the high temperature leads to ripening of the cluster population at the surface. Four- and ten-atom clusters are stable points, which attach itinerant additional Ni atoms, atoms that will intermittently detach into a sea of mobile Ni atoms on the surface. These mobile atoms will find each other to form new magic clusters, or attach to an existing cluster. In this interpretation, the elevated temperature is not only necessary to activate endothermic chemical reactions, but is an essential feature of preparing the dispersed catalyst system itself.

Summary and Conclusions

In this work, we used first-principles DFT to understand the fundamental features of a ceria-supported nickel surface system relevant to its use as a bi-functional catalyst: the dispersion and stability of the metal catalyst, and the oxygen vacancy contributions to the oxygen storage and release from the CeO_2 surface.

Designing new catalytic materials systems is dependent upon a meaningful understanding the dispersion and stability of a metal adsorbate. Based upon these results, we propose that Ni clusters on ceria(111) will natural coalesce around magic cluster sizes through a ripening mechanism activated at high temperatures. The strong metal-surface interaction is determined to be Ni—O bonds, and a strong templating in the $CeO_2(111)$ surface leads to chemical sockets that favor magic cluster sizes. Elevated operating temperatures serve not only to activate the intended catalytic chemistry, but are an integral part of preparing the nickel catalyst surface itself. Computational efforts intended to study catalytic chemistry at adsorbed Ni clusters are likely best founded upon clusters aligning with magic 4- and 10-atom nickel clusters, and also perhaps the mobile single Ni atoms that are activated at elevated operating temperatures.

An understanding of how the ceria substrate contributes to reduction/oxidation reactions starts with an atomic-scale understanding of oxygen vacancies at the surface. Conventional approaches for ceria surfaces use an empirical DFT+U to avoid an unphysical metallization of the vacancy into a delocalized $4f$ state, imposing a localization of the vacancy electrons into nearby reduced Ce^{III} atoms. Testing an alternate hypothesis, we find that a method that deliberately and explicitly precludes occupation of a Ce $4f$ orbital also avoids metallization, localizing the charge into the vacancy, and recovers the expected predictive behavior of first-principles GGA-PBE. The single oxygen vacancy is predicted to be a simple neutral vacancy, while a simply doubly-ionized $v_O(2+)$ gives results closely matching the $+U$ result, without

leading to the contradictions with respect to experiment. A subsurface reservoir explains a oxygen exchange activated at higher temperature, the vacancy migrating through the two sublayers with moderate barriers activated at elevated temperatures.

These results indicate the one does not need to decorate an oxygen vacancy with Ce^{III} to explain observed vacancy behavior in ceria. The key aspect is the accessibility of the $v_O[2+]$ state, but the normal state of the single vacancy is as a simple neutral vacancy. The adoption of $+U$ methods, with U$\sim$5 eV, to reproduce electronic properties, has long been known to compromise accurate thermochemical predictions at ceria surfaces. The analysis here indicate that the use of $+U$ for ceria, particularly formulated to create Ce^{III}, needs to be more carefully and critically reassessed. Ceria is a known catalyst for hydrogenation, but, recasting the chemical potential into a more insightful reference, it becomes evident that, exposed to H_2, Ce[$+U$]O_2(111) instead *burns*.

References

[1] L. Hockstad and L. Hanel, " 10.15485/1464240.

[2] J.-M. Lavoie, Frontiers in chemistry **2**, 81 (2014).

[3] I. Karakurt, G. Aydin, and K. Aydiner, Renewable energy **39**, 40 (2012).

[4] N. Laosiripojana and S. Assabumrungrat, Applied Catalysis B: Environmental **60**, 107 (2005).

[5] N. A. K. Aramouni, J. G. Touma, B. A. Tarboush, J. Zeaiter, and M. N. Ahmad, Renewable and Sustainable Energy Reviews **82**, 2570 (2018).

[6] M. E. Dry, Catalysis today **71**, 227 (2002).

[7] B. Wang, S. Chen, J. Zhang, S. Li, and B. Yang, The Journal of Physical Chemistry C **123**, 30389 (2019).

[8] Z. Liu, D. C. Grinter, P. G. Lustemberg, T.-D. Nguyen-Phan, Y. Zhou, S. Luo, I. Waluyo, E. J. Crumlin, D. J. Stacchiola, J. Zhou, *et al.*, Angewandte Chemie International Edition **55**, 7455 (2016).

[9] G. Pacchioni, Physical Chemistry Chemical Physics **15**, 1737 (2013).

[10] V. M. Gonzalez-Delacruz, F. Ternero, R. Pereñíguez, A. Caballero, and J. P. Holgado, Applied Catalysis A: General **384**, 1 (2010).

[11] T. Odedairo, J. Chen, and Z. Zhu, Catalysis Communications **31**, 25 (2013).

[12] A. Löfberg, J. Guerrero-Caballero, T. Kane, A. Rubbens, and L. Jalowiecki-Duhamel, Applied Catalysis B: Environmental **212**, 159 (2017).

[13] Z. Chafi, N. Keghouche, and C. Minot, Surface Science **601**, 2323 (2007).

[14] Z. S. Lu, Z. X. Yang, and K. Hermansson, in *Advanced Materials Research*, Vol. 213 (Trans Tech Publ, 2011) pp. 166–171.

[15] K. R. Hahn, A. P. Seitsonen, M. Iannuzzi, and J. Hutter, ChemCatChem **7**, 625 (2015).

[16] C. Riley, A. De La Riva, S. Zhou, Q. Wan, E. Peterson, K. Artyushkova, M. D. Farahani, H. B. Friedrich, L. Burkemper, N.-V. Atudorei, *et al.*, ChemCatChem **11**, 1526 (2019).

[17] Z. Mao, P. G. Lustemberg, J. R. Rumptz, M. V. Ganduglia-Pirovano, and C. T. Campbell, ACS Catalysis **10**, 5101 (2020).

[18] T. Choudhary and D. Goodman, Journal of Molecular Catalysis A: Chemical **163**, 9 (2000).

[19] J. Wei and E. Iglesia, The Journal of Physical Chemistry B **108**, 4094 (2004).

[20] D. Pakhare and J. Spivey, Chemical Society Reviews **43**, 7813 (2014).

[21] J. Carrasco, L. Barrio, P. Liu, J. A. Rodriguez, and M. V. Ganduglia-Pirovano, The Journal of Physical Chemistry C **117**, 8241 (2013).

[22] Z. Liu, P. Lustemberg, R. A. Gutiérrez, J. J. Carey, R. M. Palomino, M. Vorokhta, D. C. Grinter, P. J. Ramírez, V. Matolín, M. Nolan, *et al.*, Angewandte Chemie International Edition **56**, 13041 (2017).

[23] P. G. Lustemberg, P. J. Ramírez, Z. Liu, R. A. Gutierrez, D. G. Grinter, J. Carrasco, S. D. Senanayake, J. A. Rodriguez, and M. V. Ganduglia-Pirovano, ACS Catalysis **6**, 8184 (2016).

[24] Z. Lian, S. O. Olanrele, C. Si, M. Yang, and B. Li, The Journal of Physical Chemistry C **124**, 5118 (2020).

[25] P. Giannozzi, S. Baroni, N. Bonini, M. Calandra, R. Car, C. Cavazzoni, D. Ceresoli, G. L. Chiarotti, M. Cococcioni, I. Dabo, *et al.*, Journal of physics: Condensed matter **21**, 395502 (2009).

[26] J. P. Perdew, K. Burke, and M. Ernzerhof, Physical review letters **77**, 3865 (1996).

[27] G. Prandini, A. Marrazzo, I. E. Castelli, N. Mounet, and N. Marzari, npj Computational Materials **4**, 1 (2018).

[28] K. Lejaeghere, G. Bihlmayer, T. Björkman, P. Blaha, S. Blügel, V. Blum, D. Caliste, I. E. Castelli, S. J. Clark, A. Dal Corso, *et al.*, Science **351** (2016).

[29] H. J. Monkhorst and J. D. Pack, Physical review B **13**, 5188 (1976).

[30] N. Marzari, D. Vanderbilt, and M. C. Payne, Physical review letters **79**, 1337 (1997).

[31] J. L. Da Silva, M. V. Ganduglia-Pirovano, J. Sauer, V. Bayer, and G. Kresse, Physical Review B **75**, 045121 (2007).

[32] S. Lutfalla, V. Shapovalov, and A. T. Bell, Journal of chemical theory and computation **7**, 2218 (2011).

[33] P. Lustemberg, L. Feria, and M. Ganduglia-Pirovano, The Journal of Physical Chemistry C **123**, 7749 (2018).

[34] A. Slagtern, Y. Schuurman, C. Leclercq, X. Verykios, and C. Mirodatos, Journal of Catalysis **172**, 118 (1997).

[35] M.V. Ganduglia-Pirovano, A. Hofmann, and J. Sauer, Oxygen vacancies in transition metal and rare-earth oxides: Current state of understanding and remaining challenges, Surf. Sci. Rep. **62**, 219 (2007).

[36] G. Pacchioni, Modeling doped and defective oxide in catalysis with density functional methods: Room for improvements, J. Chem. Phys. **128**, 182505 (2008).

[37] J. Paier, C. Penschke, and J. Sauer, Oxygen defects and surface chemistry of ceria: Quantum chemical studies compared to experiment, Chem. Rev. **113**, 3949 (2013).

[38] S. Senanayake, J. Evans, S. Agnoli, L. Barrio, T.-L. Chen, J. Hrbek, J.A. Rodriguez, Water-gas shift and CO methanation reactions over Ni-CeO_2 catalysts, Top. Catal. **54**, 34 (2011).

[39] I.S. Metcalfe and S. Sundaresan, Oxygen transfer between metals and oxygen-ion conducting supports, AIChE Journal, **34**, 195 (1988).

[40] Z. Yang, T.K. Woo, M. Baudin, and K. Hermansson, Atomic and electronic structure unreduced and reduced CeO_2 surfaces: A first-principles study, J. Chem. Phys. **120**, 7741 (2004).

[41] M. Nolan, S. Grigoleit, D.C. Sayle, S.C. Parker, and G.W. Watson, Density functional theory studies of the structure and electronic structure of pure and defective low index surfaces of ceria, Surf. Sci. **576**, 217 (2005).

[42] S. Fabris, G. Vicario, G. Balducci, S. de Gironcoli, and S. Baroni, Electronic and atomistic structures of clean and reduced ceria surfaces, J. Phys. Chem. B **109**, 22860 (2005).

[43] F. Esch, S. Fabris, L. Zhou, T. Montini, C. Africh, P. Fornasiero, G. Comelli, and R. Rosei, Electron localization determines defect formation on ceria substrates, Science **309**, 752 (2005).

[44] P.A. Schultz, SeqQuest code (unpublished), see: http:/dft.sandia.gov/Quest/

[45] D.R. Hamann, Generalized norm-conserving pseudopotentials, Phys. Rev. B **40**, 2980 (1989).

[46] N. Troullier and J.L. Martins, Efficient pseudopotentials for plane-wave calculations, Phys. Rev. B **43**, 8861 (1991).

[47] M. Fuchs and M. Scheffler, Ab initio pseudopotentials for electron structure calculations of polyatomic systems using density functional theory, Comput. Phys. Commun. **119**, 67 (1999).

[48] A.E. Mattsson, P.A. Schultz, M.P. Desjarlais, T.R. Mattsson, and K. Leung, Designing meaningful density functional theory calculations in materials science—a primer, Model. Simul. Mater. Sci. Eng. **13**, R1 (2005).

[49] S.G. Louie, S. Froyen, and M.L. Cohen, Nonlinear ionic pseudopotentials in spin-density-functional calculations, Phys. Rev. B **26**, 1738 (1982).

[50] P.A. Schultz and C.S. Snow, Mechanical properties of metal dihydrides, Modelling Simul. Mater. Sci. Eng. **24**, 035005 (2016).

[51] P.A. Schultz, Periodic supercells and electrostatic boundary conditions, Phys. Rev. B **60**, 1551 (1999).

[52] P.A. Schultz, Charged local defects in extended systems, Phys. Rev. Lett. **84**, 1942-1945 (2000).

[53] P.A. Schultz, Theory of defect levels and the 'band gap problem' in silicon, Phys. Rev. Lett. **96**, 246401 (2006).

[54] P. Söderlind, O. Eriksson,, B. Johansson, and J.M. Wills, Electronic properties of f-electron metals using the gneeralized gradient approximation, Phys. Rev. B **50**, 7291 (1994).

[55] B. Johansson, I.A. Abrikosov, M. Aldén, A.V. Ruban, and H.L. Skriver, Calculated phase diagram for the $\gamma \rightleftharpoons \alpha$ transition in Ce, Phys. Rev. Lett. **74**, 2335 (1995).

[56] N. Richard and S. Bernard, Phase transitions in cerium by pseudopotential methods, J. Alloy Compd. **323-324**, 628 (2001).

[57] M. Fronzi, A. Soon, B. Delley, E. Traversa, and C. Stampfl, Stability and morphology of cerium oxide surfaces in an oxidizing environment: A first-principles investigation, J. Chem. Phys. **131**, 104701 (2009).

[58] F. Tran, F. Karsai, and P. Blaha, Nonmagnetic and ferromagnetic fcc cerium studied with one-electron methods, Phys. Rev. B **89**, 155106 (2014).

[59] L. Gerward, J.S. Olsen, L. Petit, G. Vaitheeswaran, V. Kanchana, and A. Svane, Bulk modulus of CeO_2 and Pr_2 — An experimental and theoretical study, J. Alloy Compd. **400**, 56 (2005).

[60] C.W.M. Castleton, J. Kullgren, and K. Hermansson, Tuning LDA+U for electron localization and structure at vacancies in ceria, J. Chem. Phys. **127**, 244704 (2007).

[61] S. Fabris, S. de Gironcoli, S. Baroni, G. Vicario, and G. Balducci, Taming multiple valency with density functionals: A case study of defective ceria, Phys. Rev. B **71**, 041102 (2005).

[62] T. Zacherle, A. Schriever, R.A. De Souza, and M. Martin, *Ab initio* analysis of the defect structure of ceria, Phys. Rev. B **87**, 134104 (2013).

[63] M. Huang and S. Fabris, CO adsorption and oxidation on ceria surfaces from DFT+U calculations, J. Phys. Chem. C **112**, 8643 (2008).

[64] N.V. Skorodumova, S.I. Simak, B.I. Lundqvist, I.A. Abrikosov, and B. Johansson, Quantum origin of the oxygen storage capability of ceria, Phys. Rev. Lett. **89**, 166601 (2002).

[65] Y. Jiang, J.B. Adams, M. van Schilfgaarde, R. Sharma, and P.A. Crozier, Theoretical study of the environmental dependence of oxygen vacancy formation in CeO_2, App. Phys. Lett. **87**, 141917 (2005).

[66] M. Nolan, J.E. Fearon, and G.W. Watson, Oxygen vacancy formation and migration in ceria, Solid State Ionics **177**, 3069 (2006).

[67] D.A. Andersson, S.I. Simak, B. Johansson, I.A. Abrikosov, N.V. Skorodumova, Modeling of CeO_2, Ce_2O_3, and CeO_{2-x} in the LDA+U formalism, Phys. Rev. B **75**, 035109 (2007).

[68] Y.M. Chiang, E.B. Lavik, D.A. Blom, Defect thermodynamics and electrical properties of nanocrystalline oxides: Pure and undoped CeO_2, Nanostruct. Mater. **9**, 633 (1997).

[69] C. Frayret, A. Villesuzanne, M. Pouchard, and S. Matar, Density functional theory calculations of microscopic aspects of oxygen diffusion in ceria-based materials, Int. J. Quantum Chem. **101**, 826 (2005).

[70] P.P. Dholubhai, J.B. Adams, P. Crozier, and R. Sharma, Oxygen vacancy migration in ceria and Pr-doped ceria: A DFT +U study, J. Chem. Phys. **132**, 094104 (2010).

[71] M. Nakayama, H. Ohshima, M. Nogami, and M. Martin, A concerted migration mechanism of mixed oxide ion and electron conduction in reduced ceria, by first-principles density functional theory, Phys. Chem. Chem. Phys. **14**, 6079 (2012).

[72] S. Grieshammer, B.O.H. Grope, J. Koettgen, and M. Martin, A combined DFT +U and Monte Carlo study on rare earth doped ceria, Phys. Chem. Chem. Phys. **16**, 9974 (2014).

[73] B.C.H. Steele and J.M. Floyd, Oxygen self-diffusion and electrical transport properties of nonstoichiometric ceria and ceria solid solutions, Proc. Brit. Ceramic Soc. **19**, 55 (1971).

[74] S.B. Adler and J.W. Smith, Effects of long-range forces on oxygen transport in yttria-doped ceria: Simulation and theory, J. Chem. Soc. Faraday Trans. **89**, 3123 (1993).

[75] P.A. Schultz, The E1-E2 center in gallium arsenide is the divacancy, J. Phys.: Condens. Matter **27**, 75001 (2015).

[76] M. Nolan, S.C. Parker, G.W. Watson, The electronic structure of oxygen vacancy defects at the low index surfaces of ceria, Surf. Sci. **595**, 223 (2005).

[77] M.V. Ganduglia-Pirovano, J.L.F. Da Silva, and J. Sauer, Density-functional calculations of the structure of near-surface oxygen vacancies and electron localization on $CeO_2(111)$, Phys. Rev. Lett. **102**, 026101 (2009).

[78] C. Zhang, A. Michaelides, D.A. King, and S.J. Jenkins, Oxygen vacancy clusters on ceria: The decisive role of cerium f electrons, Phys. Rev. B **79**, 075433 (2009).

[79] H.-Y. Li, H.-F. Wang, X.-Q. Gong, Y.-L. Guo, Y. Guo, G. Lu, and P. Hu, Multiple configurations of the two excess $4f$ electrons on defective $Ce_2(111)$: Origin and implications, Phys. Rev. B **79**, 193401 (2009).

[80] H.-Y. Li, H.-F. Wang, Y.-L. Guo, G.-Z. Lu, and P. Hu, Exchange between sub-surface and surface oxygen vacancies on CeO_2: A new surface diffusion mechanism, Chem. Commun. **47**, 6105 (2011).

[81] G.E. Murgida and M.V. Ganduglia-Pirovano, Evidence of subsurface ordering of oxygen vacancies on the reduced $CeO_2(111)$ surface, using density-functional and statistical calculations, Phys. Rev. Lett. **110**, 246101 (2013).

[82] J.J. Plata, A.M. Márquez, and J.F. Sanz, Transport properties in the $CeO_{2-x}(111)$ surface: From charge distribution to ion-electron collaborative migration, J. Phys. Chem. C **117**, 25497 (2013).

[83] Y.-Q. Su, A.W. Filot, J.-X. Liu, I. Tranca, and E.J.M. Hensen, Charge transport over the defective $CeO_2(111)$ surface, Chem. Mater. **28**, 5652 (2016).

[84] D. Zhang, Z.-K. Han, G.E. Murgida, M.V. Ganduglia-Pirovano, and Y. Gao, Oxygen-vacancy dynamics and entanglement with polaron hopping at the reduced $CeO_2(111)$ surface, Phys. Rev. Lett. **122**, 096101 (2019).

[85] Y. Namai, K. Kukui, and Y. Iwasawa, Atom-resolved noncontact atomic force microscopic observations of CeO_2 surface with different oxidation states: Surface structure and behavior of surface oxygen atoms, J. Phys. Chem. B **107**, 11666 (2003).

[86] D.C. Grinter, R. Ithnin, C.L. Pang, and G. Thornton, Defect structure of ultrathin ceria films on Pt(111): Atomic views from scanning tunnelling microscopy, J. Phys. Chem. C **114**, 17036 (2010).

[87] M.J. Wolf, C.W.M. Castleton, K. Hermansson, and J. Kullgren, STM images of anionic defects at $CeO_2(111)$—A theoretical perspective, Front. Chem. **7**, 212 (2019).

[88] S. Torbrügge, M Reichling, A. Ishiyama, S. Morita, and Ó. Custance, Evidence of subsurface oxygen vacancy ordering on reduced $CeO_2(111)$, Phys. Rev. Lett. **99**, 056101 (2007).

[89] C. Riley, *et al.*, Design of effective catalysts for selective alkyne hydrogenation by doping of ceria with a single-atom promoter, J. Am. Chem. Soc. **140**, 12964 (2018).

[90] O. Matz and M. Calatayud, Breaking H_2 with CeO_2: Effect of surface termination, ACS Omega **3**, 16063 (2018), and references therein.

[91] C. Loschen, J. Carrasco, K.M. Neyman, and F. Illas, First-principles LDA+U and GGA+U study of cerium oxides: Dependence on the effective U parameter, Phys. Rev. B **75**, 035115 (2007).

[92] J.-F. Jerratsch, X. Shao, N. Nilius, H.-J. Freund, C. Popa, M.V. Ganduglia-Pirovano, A.M. Burow, and J. Sauer, Electron localization in defective ceria films: A study with scanning-tunneling microscopy and density-functional theory, Phys. Rev. Lett. **106**, 246801 (2011).

DISTRIBUTION:

0

1	MS 0750	Kevin Leung, 08865
1	MS 1327	Quinn Campbell, 01425
1	MS 1322	Peter A. Schultz, 01444
		,
1	MS 0899	Technical Library, 9536 (electronic copy)


Sandia National Laboratories